Research Square

Preprints are preliminary reports that have not undergone peer review.
They should not be considered conclusive, used to inform clinical practice,
or referenced by the media as validated information.

A Comparative Floquet–Lyapunov Study of Perturbation-Induced Halo Orbit Instability in the Earth–Moon System

Ambrose Osadugba
Space Generation Advisory Council
Samuel Oyefusi
sooyefusi@wpi.edu
Worcester Polytechnic Institute

Research Article

Keywords: Cislunar dynamics, Perturbation ranking, Halo orbit stability, Third-body effects, SRP, Station-keeping

Posted Date: September 25th, 2026

DOI: https://doi.org/10.21203/rs.3.rs-11002775/v1

License: This work is licensed under a Creative Commons Attribution 4.0 International License.
Read Full License

Additional Declarations: No competing interests reported.

A Comparative Floquet–Lyapunov Study of Perturbation-Induced Halo Orbit Instability in the Earth–Moon System

PRINCIPAL AUTHOR

Ambrose Osadugba.
SGAC Member,
Akure, Nigeria.
ambrosekamzy@gmail.com

CORRESPONDING AUTHOR

Samuel Oyefusi.
Department of Robotics Engineering,
Worcester Polytechnic Institute, USA.
sooyefusi@wpi.edu

ABSTRACT

Halo orbits around the Earth–Moon L1–L3 underpin near-term cislunar infrastructure, from the Artemis Lunar Gateway to lunar communication relays, yet their operational viability depends on how strongly non-idealized forces reshape their intrinsic instability. While the linear stability of these orbits in the Circular Restricted Three-Body Problem (CRTBP) is well established, the relative impact of the perturbations a real mission actually encounters (solar radiation pressure, lunar oblateness, Earth's albedo and thermal radiation, and third-body solar gravity) has not been systematically ranked within a single, self-consistent framework. This study addresses that gap. Numerically refined halo orbits at L1–L3 are constructed via Richardson third-order approximations and single-shooting differential correction (periodicity errors $< 10^{-10}$; Jacobi deviations $< 10^{-12}$), then subjected to a unified Floquet–Lyapunov analysis under each perturbation. Linear stability is quantified through the monodromy matrix and Floquet multipliers; nonlinear behavior is probed through Poincaré maps and Lyapunov exponents; and sensitivity thresholds are mapped via Monte-Carlo sampling of initial conditions. The comparative results yield a clear hierarchy: third-body solar gravity dominates, driving Floquet-multiplier shifts of up to 88% and collapsing the L1 maximum exponent from 0.4783 to 0.2003; SRP and lunar J2 act as mild regularizers, reducing chaotic divergence at L1 and L2 while leaving L3 largely unaffected; Earth's albedo produces only marginal shifts across all three orbits. The dominance of solar gravity is shown to be the operative constraint on unmaintained cislunar station-keeping, and L3 is identified as the quasi-stable exception, requiring substantially less frequent correction than L1 and L2. Results are benchmarked against Jorba & Masdemont (1999), Kolemen et al. (2012), and Richardson (1980), with future extensions to full-ephemeris models identified as the next step toward mission-grade fidelity.

Keywords: Cislunar dynamics; Perturbation ranking; Halo orbit stability; Third-body effects; SRP; Station-keeping

1.0 INTRODUCTION

1.1. BACKGROUND AND MOTIVATION

The next decade of cislunar activity will be built on halo orbits. NASA's Artemis Lunar Gateway is planned to occupy a near-rectilinear halo orbit (NRHO) around the Earth–Moon L2; China's Queqiao relay satellite already operates on a halo orbit at the same libration point to sustain communications with the far-side Chang'e lunar surface missions; and multiple proposed telescope, communication-relay, and deep-space staging concepts assume the same class of orbit as their operational home. What makes these orbits attractive, namely their capacity to hold a spacecraft in a quasi-stable geometric relationship with both primary bodies for minimal propellant expenditure, is also what makes their stability analysis operationally consequential rather than merely academic. Every station-keeping burn, every mission-duration estimate, and every fuel-budget allocation for a cislunar asset depends on how accurately the instability of its host orbit is quantified.

The mathematical setting is the Circular Restricted Three-Body Problem (CRTBP), where a spacecraft of negligible mass moves under the gravitational influence of two primaries, here the Earth and the Moon, in mutual circular orbit about their barycenter. Within this framework, halo orbits are the three-dimensional periodic solutions that bifurcate from the planar Lyapunov family at the collinear Lagrange points L1–L3. They were first constructed analytically by Farquhar (1970) and refined into the numerically periodic families used today by Richardson (1980) and Howell (1984). Their linear stability structure, comprising hyperbolic instability at L1 and L2 and milder instability at L3, has been characterized since Jorba and Masdemont (1999) formalized the center-manifold reduction, and successive studies have layered increasingly sophisticated tools on top: multiple Poincaré-section methods for detecting quasi-periodic families (Kolemen et al., 2012), Jacobi-stability formulations for perturbed regimes (Blaga et al., 2021), and high-order analytical continuations near triangular points (Lei and Xu, 2013). Station-keeping frameworks built on this foundation now include suboptimal nonlinear model predictive control for NRHOs (Berning et al., 2020) and manifold-based rendezvous strategies (Sato et al., 2015).

Against this well-developed backdrop, a specific gap remains open. Individual perturbations acting on halo orbits have been studied in isolation: solar radiation pressure by Heiligers et al. (2015) and Sheth and O (2020), lunar oblateness and photo-gravitational effects by Chidambararaj and Sharma (2016), and full-ephemeris third-body dynamics by Chen et al. (2011) and Dong et al. (2024). However, the relative contribution of these forces to halo-orbit instability, evaluated within one self-consistent Floquet–Lyapunov framework and across all three collinear libration points, has not been systematically established. Mission designers currently reason about perturbation priority from qualitative intuition or piecemeal comparison across incompatible modeling assumptions. For an era in which cislunar orbits are transitioning from analytical constructs to operational infrastructure, that gap has practical cost: it determines which perturbations must be modeled to fidelity in mission planning and which can be safely neglected in first-order station-keeping budgets.

This study addresses that gap directly. Numerically refined halo orbits at Earth–Moon L1, L2, and L3 are subjected to a unified stability assessment combining Floquet-multiplier analysis (linear) with Poincaré-section and Lyapunov-exponent diagnostics (nonlinear), then re-evaluated under solar radiation pressure, lunar oblateness (J2), Earth's albedo and thermal radiation, and third-body solar gravity, each perturbation applied independently within the same modeling framework, with results benchmarked against the classical unperturbed baseline. The output is a quantitative ranking of perturbation impact across the collinear halo family, complemented by Monte-Carlo sensitivity maps identifying the initial-condition thresholds at which linear stability estimates lose predictive value. The intent is not to introduce new stability tooling, since the Floquet apparatus is classical, but to close the comparative gap that operational cislunar mission design requires.

1.2. OBJECTIVES OF THE STUDY

The overarching aim of this work is to establish a quantitative, self-consistent ranking of perturbation impacts on the linear and nonlinear stability of Earth–Moon halo orbits at L1–L3. Four specific objectives support this aim:

a) To construct numerically refined halo orbits at each of the collinear Lagrange points L1, L2, and L3 to a fidelity sufficient for stability analysis, verified through periodicity and Jacobi-constant conservation metrics.

b) To characterize the baseline stability of these orbits within the Circular Restricted Three-Body Problem using a unified Floquet–Lyapunov framework, combining monodromy-matrix eigenstructure analysis with Poincaré-section and Lyapunov-exponent diagnostics, thereby capturing both linear and nonlinear stability behavior within one methodological setting.

c) To quantify and compare the effects of four perturbations (solar radiation pressure, lunar oblateness, Earth's albedo and thermal radiation, and third-body solar gravity) on the same baseline orbits, using identical numerical settings so that the resulting shifts in Floquet multipliers and Lyapunov exponents can be directly compared.

d) To map the sensitivity of the stability results to variations in initial conditions through Monte-Carlo analysis, identifying the thresholds beyond which linear stability estimates cease to be predictive and characterizing the resulting implications for orbit selection and station-keeping cadence in cislunar mission design.

1.3. LITERATURE REVIEW

Halo orbit studies around the Earth–Moon Lagrange points L1, L2, and L3 constitute a critical field within astrodynamics, offering stable platforms for lunar missions, deep-space astronomy, and interplanetary transfer. These time-periodic solutions in the CRTBP are particularly valuable because they are quasi-stable and need minimal fuel to station-keep. Nevertheless, their stability requires thorough examination. Floquet theory, a methodology that assesses stability through monodromy matrices and Floquet multipliers, has become a cornerstone for understanding orbital perturbations and designing control schemes in the Earth–Moon system.

Halo orbits are bifurcations of planar Lyapunov orbits around the collinear Lagrange points in the CRTBP, where a massless particle (e.g., spacecraft) revolves under the gravitational influence of two primaries (Earth and Moon) (Richardson, 1980). In the Earth–Moon case, these orbits are influenced by the system's mass ratio ($\mu \approx 0.01215$) and are out-of-plane, making them ideal for missions such as lunar gateways (Whitley & Martinez, 2016). Initial work by Farquhar (1970) laid the groundwork for halo orbit dynamics, and recent studies have expanded this to perturbed environments, including solar radiation pressure and lunar eccentricity (Heiligers et al., 2015; Wawrzyniak & Howell, 2011).

Numerical techniques are required to create precise halo orbits, commonly beginning with analytical approximations and refining through differential corrections (Howell, 1984). For example, Calleja et al. (2012) utilized boundary-value problem formulations to calculate invariant manifolds and connecting orbits, illustrating numerical continuation refinement of halo families near L1 and L2. In the Earth–Moon system, Liu et al. (2019) investigated resonant orbits, illustrating that variations in initial parameters result in varied halo configurations. Recent refinements include full-ephemeris models that incorporate non-circular lunar motion and third-body perturbations (Chen et al., 2011; Dong et al., 2024). These dynamics highlight requirements for stability tools such as Floquet analysis in order to quantify sensitivity to initial conditions.

Floquet theory is an effective tool for stability analysis of periodic orbits through linearization of the equations of motion and calculation of the monodromy matrix, whose eigenvalues (Floquet multipliers) determine stability (Floquet, 1883). Multipliers with a magnitude greater than unity indicate instability, as is typical of halo orbits around L1 and L2, whereas those close to unity imply quasi-stability (Langford & Weiss, 2023). The method has developed from linearization to nonlinear extensions, which allow for exact quantification of instability.

In the Earth–Moon system, Floquet multipliers have been used to classify families of halo orbits. Center-manifold reductions were introduced by Jorba and Masdemont (1999), combining Floquet analysis with numerical continuation to characterize Lissajous and halo orbits. Recent research has built on this groundwork: Kolemen et al. (2012) used multiple Poincaré sections combined with Floquet theory to distinguish quasi-periodic orbits, thereby revealing stability thresholds for L1 halo orbits. Blaga et al. (2021) applied Jacobi stability analysis, including Floquet multipliers, to study perturbations within the Circular Restricted Three-Body Problem (CRTBP), proving that halo orbits around L1 exhibit conditional stability under small perturbations.

Numerical refinement enhances Floquet analysis by applying iterative orbit corrections to satisfy periodicity constraints. Korneev and Aksenov (2021) presented algorithms specifically designed for libration point orbits, using Floquet multipliers to assess stability for refined halo orbits in perturbed models. Similarly, Marsola et al. (2021) refined halo orbits about L1 and L2 via differential corrections, making use of Floquet theory to develop station-keeping controllers to counteract instabilities. With regard to L3, which is less unstable, Alrebdi et al.

(2022) studied equilibrium points and periodic networks in the context of the pseudo-Newtonian Circular Restricted Three-Body Problem (CRTBP), using Floquet exponents to highlight chaotic domains. Recent studies have incorporated solar perturbations: Sheth and O (2020) studied the effect of photogravitational forces on L1/L2 halos, performing numerical refinements of orbits while determining stability via Floquet multipliers, concluding that oblateness reduces stability margins.

Higher refinements involve high-order analytical solutions and machine learning assists. Lei and Xu (2013) developed high-order solutions for triangular libration points, validating stability after refinement using Floquet theory. Gao and Wang (2020) presented several time-scale solutions for CRTBP, refining L1 halos using Floquet-based measures. In a 2023 paper, Sirbu and Leonardi refined autonomous navigation halo orbits, using Floquet multipliers to confirm synchronization stability. These studies highlight that numerical refinement, usually through shooting methods or collocation, enhances Floquet accuracy for the prediction of long-term behavior (Haapala & Howell, 2014; Ribeiro et al., 2022).

Floquet-based stability guides control approaches for halo orbit maintenance. Berning et al. (2020) illustrated suboptimal nonlinear model predictive control (NMPC) for Near Rectilinear halo orbits (NRHOs) tracking around L1/L2, employing Floquet multipliers to address constraints and perturbations. Sato et al. (2015) used invariant manifolds and Floquet analysis for spacecraft rendezvous in halo orbits, optimizing trajectories for fuel efficiency.

Applications include mission design: Burns et al. (2019) suggested low-latency telerobotics from L2 halos, based on Floquet-stabilized orbits for lunar surface operations. Santana-Ros et al. (2022) described Earth Trojan asteroids near L4/L5, applying Floquet theory to determine orbital stability. In solar sails, Heiligers et al. (2015) and Sood & Howell (2016) developed halo transfers, incorporating Floquet multipliers to determine stability under propulsion. Hysa (2024) studied nonlinear dynamics near L4/L5, using Floquet analysis for chaotic motions in Earth–Moon and Sun–Earth systems.

Recent studies integrate Floquet theory with hybrid models. Archambeau et al. (2011) analyzed eight-shaped Lissajous orbits, stabilizing through Floquet exponents. Tang (2019) employed Koopman reduced-order control for the CRTBP, using Floquet metrics to verify stabilization. Yan (2020) stabilized L1 through Port-Hamiltonian approaches, confirming the result through Floquet multipliers. These approaches underscore Floquet's utility in optimizing orbits for missions such as Artemis (Williams et al., 2017).

Further research extends Floquet applications to perturbed regimes. Chidambararaj and Sharma (2016) studied photo-gravitational halos with oblateness, applying Floquet theory for Sun–Earth system stability. Abouelmagd et al. (2023) studied perturbed orbits, extending Floquet analysis to two- and three-body problems. Dong et al. (2024) compared Moon-based and L1 observations, using implicitly Floquet-inspired metrics for orbital refinement. Lizy-Destrez et al. (2019) and Slíz-Balogh et al. (2022) applied Floquet to rendezvous and dust cloud dynamics in the vicinity of Lagrange points.

Floquet-based stability theory, in combination with numerical refinement, offers a powerful toolset to analyze halo orbits in Earth–Moon Lagrange points. By computing monodromy matrices and multipliers, researchers can predict instabilities, refine orbits, and design control laws for missions. As computational tools improve, the combination of Floquet theory and AI-assisted refinement is expected to increase accuracy, paving the way for future missions in cislunar space.

Taken together, this body of work establishes Floquet-based stability analysis as a mature and reliable tool for characterizing halo-orbit dynamics and confirms that each of the perturbations relevant to cislunar operations (solar radiation pressure, lunar oblateness, Earth's albedo, and third-body solar gravity) has been examined in some form. What has not been undertaken, however, is a study that evaluates all four of these perturbations within a single unified Floquet–Lyapunov framework, applied consistently to the L1, L2, and L3 halo families, using identical numerical settings and validation metrics. Prior comparisons across perturbations are unavoidably indirect: they draw on results produced under different orbital families, different levels of numerical refinement, different stability diagnostics, and different underlying dynamical models. This heterogeneity is not a criticism of the individual works, each of which was designed to answer a different question, but it does mean that the

relative ordering of perturbation impacts on cislunar halo-orbit stability is not currently established on a like-for-like basis. The remainder of this study is directed at that specific question.

2.0 ORBITAL MECHANICS: LAGRANGE POINTS AND HALO ORBITS

Orbital mechanics, the foundational building block of modern astrodynamics and spacecraft navigation, describes how celestial bodies interact under gravitational forces. The motion of natural and artificial satellites is governed by Newton's laws of motion, further refined by advanced computational and dynamical models such as the Three-Body Problem (3BP). In the context of space missions within the Earth–Moon system, understanding the behavior of the points at which the gravitational influences of the Earth and the Moon reach equilibrium (i.e., the Lagrange points) is crucial to the analysis of the periodic orbits used in cislunar missions. This section reviews the fundamentals of orbital mechanics, focusing on the Restricted Three-Body Problem (R3BP), the mathematical equilibria that give rise to the Lagrange points, and the theoretical and numerical background of a common class of such periodic orbits: halo orbits.

2.1. BASIC CONCEPTS IN ORBITAL MECHANICS

The study of orbital motion is governed largely by Newtonian mechanics, which encompasses Newton's three laws of motion and the law of universal gravitation; together these provide the foundation for analyzing the interaction of celestial objects under gravity.

- **Newton's First Law**: A body at rest or in uniform motion remains at rest or in uniform motion unless acted upon by an external force. This is the Law of Inertia.
- **Newton's Second Law**: The force acting on a body is equal to the rate of change of its momentum.

$$F = ma$$

- **Newton's Third Law**: For every action, there is a corresponding equal and opposite reaction.
- **Newton's Law of Universal Gravitation**: The force F acting between two bodies is directly proportional to the product of their masses m_1 and m_2 and inversely proportional to the square of the distance r between them. Mathematically, this law can be written as;

$$F = G\frac{m_1 m_2}{r^2}$$

Where G is the gravitational constant.

These principles serve as the basis for analyzing the fundamental problems of Orbital Mechanics; the Two-body and Three-body Problems.

2.1.1. The Two-body Problem (2BP)

In the Two-body problem, the two masses involved orbit their barycenter in conic trajectories under mutual gravitational attraction. This gives rise to Keplerian motion, particularly when one object is significantly more massive than the other. Keplerian motion is governed by Kepler's laws, which state that:

- A satellite orbits in an ellipse with the central object at one focus (Law of Elliptical Orbits).
- A line joining the satellite and the central body sweeps out equal areas in equal times, meaning that the satellite will move faster when it approaches the primary (Law of Equal Areas).
- The square of a satellite's orbital period, T, is directly proportional to the cube of its semi-major axis, a (Harmonic Law).

$$T^2 \propto a^3$$

However, in systems containing three or more bodies, closed-form analytical solutions of this kind are generally unobtainable. Because real-world orbital dynamics frequently involve such systems, additional perturbation models and approximations are required.

2.1.2. The Three-Body Problem (3BP) and Restricted Three-Body Problem (R3BP)

Unlike the two-body problem, the three-body problem describes the motion of three bodies under mutual gravitational influence, but it is generally unsolvable in closed analytical form. This motivates a simplified formulation better suited to orbital-mechanics analysis: the Restricted Three-Body Problem (R3BP).

In the R3BP, two massive objects move about their center of mass in circular orbits. A third body (for example, a spacecraft) of negligible mass then moves under the gravitational influence of the two primaries without appreciably affecting their motion. The R3BP is usually formulated in a rotating reference frame, in which the primaries are fixed, and the spacecraft is subject to gravitational forces together with the fictitious centrifugal and Coriolis forces. These forces are used to derive the equations of motion in the R3BP, given by:

$$\ddot{x} - 2\dot{y} = \frac{\partial U}{\partial x}, \qquad \ddot{y} + 2\dot{x} = \frac{\partial U}{\partial y}, \qquad \ddot{z} = \frac{\partial U}{\partial z}$$

Where U is the effective potential, or pseudo-potential function, usually a function of x, y, and z, given as;

$$U = \frac{1}{2}(x^2 + y^2) + \frac{1-\mu}{r_1} + \frac{\mu}{r_2}$$

Where r_1 and r_2 are the distances of the third body from each primary.

The circular R3BP admits a first integral of motion, the Jacobi constant CJ, which is conserved along the entire trajectory. The Jacobi constant is given by:

$$C_J = 2U - (\dot{x}^2 + \dot{y}^2 + \dot{z}^2)$$

The Jacobi constant is useful for defining surfaces of zero-velocity, which dictates the regions of motion of the spacecraft. Lower C_J values permit motion close to the primary objects, but higher C_J values will restrict the spacecraft's trajectory to distant regions. Coordinate system selection is crucial: Inertial frames simplify the underlying equations but obscure equilibrium points, whereas the rotating frame (aligned with the Earth–Moon line) reveals Lagrange points and periodic orbits more effectively. Transformations between frames account for time-dependent rotations, which can complicate stability analyses but highlight symmetries in the CR3BP, such as time-reversal invariance under $(t, x, y, z, \dot{x}, \dot{y}, \dot{z}) \rightarrow (-t, x, -y, z, -\dot{x}, \dot{y}, -\dot{z})$.

2.2. LAGRANGE POINTS AND THEIR PROPERTIES

Lagrange points are special locations, usually termed equilibrium solutions, in the R3BP where the gravitational forces of the two primary bodies and the centrifugal force in the rotating reference frame exactly cancel out. In cislunar space, five of these points exist.

- L1 is located along the Earth–Moon axis, between the two bodies.
- L2 is situated beyond the Moon, also along the Earth–Moon axis.
- L3 is situated on the Earth side, opposite the orbital path of the Moon.
- L4 and L5 lead and trail the Moon's orbit, forming equilateral triangles with both bodies.

L1–L3 are often considered collinear points because equilibrium is reached when there is no net acceleration, and their positions are obtained by solving the force balance equation along the Earth–Moon axis.

The balance in L4 and L5 is obtained from the combined gravity pull of Earth and Moon and the Coriolis Effect. Stability is obtained only when the mass ratio μ < 0.0385. In another form,

$$\frac{m_{Moon}}{m_{Earth} + m_{Moon}} < \frac{1}{26}$$

Since μ is approximately 0.01215 for cislunar space, L4 and L5 are often considered conditionally stable, which is also due to the absence of significant perturbations and presence of sufficient Coriolis forces. L1–L3 are unstable owing to the saddle-shaped effective potential and therefore require active stabilization through thruster firings or orbital corrections.

To mathematically obtain the Lagrange points, we solve the equations;

$$\frac{\partial U}{\partial x} = 0, \qquad \frac{\partial U}{\partial y} = 0, \qquad \frac{\partial U}{\partial z} = 0$$

The solutions to these equations yield the equilibrium positions in the rotating reference frame.

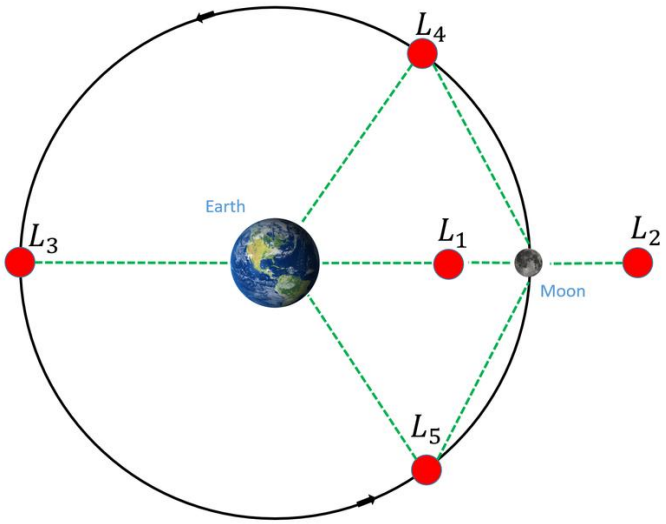


Fig. 1: Lagrange Points within the Earth–Moon system.

2.3. PERIODIC ORBITS AROUND LAGRANGE POINTS

Instead of maintaining a stationary position, spacecraft typically move in periodic or quasi-periodic orbits about the Lagrange points as a consequence of small displacements near the collinear points. Such orbits include Halo, Lyapunov and Lissajous orbits. Halo orbits are largely three-dimensional periodic orbits perpendicular to the Earth–Moon plane, particularly induced by the unstable nature of L1–L3. These orbits are usually maintained

via station-keeping maneuvers or natural dynamics, making them ideal for stationing spacecraft near Lagrange points.

2.4. HALO ORBITS IN THE CIRCULAR RESTRICTED THREE-BODY PROBLEM

Halo orbits are three-dimensional, non-planar orbits, existing in the Circular Restricted Three-Body Problem (CR3BP) and found principally around the collinear Lagrange points (L1–L3) in any two-primary system in space where the gravitational and centrifugal forces cancel out in a rotating reference frame. Unlike classical Keplerian orbits and Lyapunov orbits lying in the Earth–Moon equatorial plane, halo orbits exhibit out-of-plane motion, forming distinctive halo-shaped paths when projected onto rotating or inertial frames, which is due to the nonlinear dynamics of the CR3BP.

Halo Orbits were first proposed by Robert W. Farquhar in 1968 as a means of placing spacecraft in continuous view of both the Earth and the Moon. With the development of numerical and analytical methods, the existence and stability properties of halo orbits have been refined and actively exploited in modern space missions such as the James Webb Space Telescope, the proposed Artemis Lunar Gateway, and the Solar and Heliospheric Observatory (SOHO).

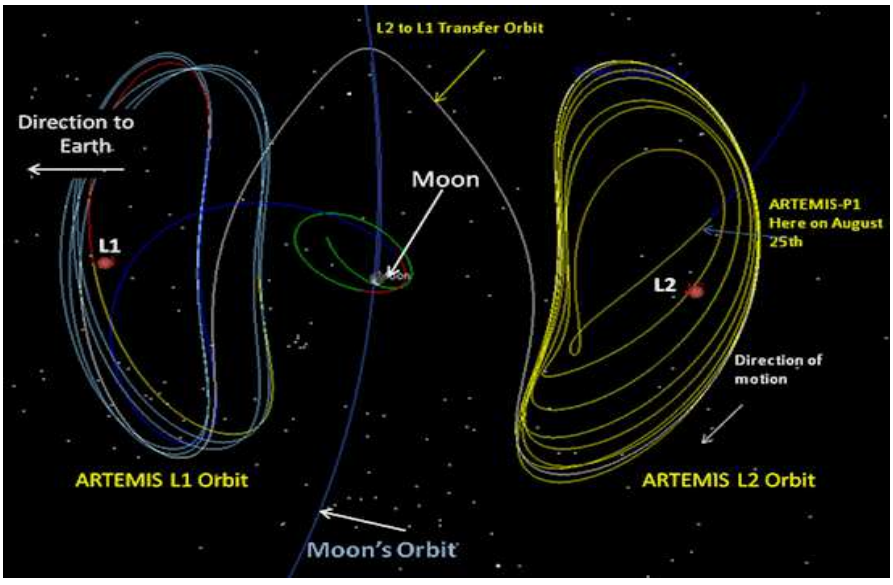


Fig. 2: Halo Orbits around Earth–Moon L1 and L2.

2.4.1. Classification of Halo Orbits

Halo orbits can be classified based on their orientation (location and vertical displacement relative to the plane of motion of the two primaries) and their size (based on amplitude along the z-axis).

By classification based on vertical displacement, we have the Northern halo orbits (where trajectory remains predominantly above the primary plane), and the Southern halo orbits (where trajectory remains predominantly below the primary plane). The classification of halo orbits based on location yields three types; L1 halo orbits (around L1 Lagrange point), L2 halo orbits (around L2), and L3 halo orbits (around L3).

Classified by size, halo orbits fall into two groups: small-amplitude halo orbits, which remain close to the Lagrange point, exhibit better long-term stability, and require less frequent station-keeping; and large-amplitude halo orbits, which extend farther from the libration point and incur substantially higher station-keeping costs.

2.4.2. In-Space Application of Halo Orbits

Due to their unique dynamical properties, halo orbits have been extensively employed in diverse space missions. Telescopes are often placed in halo orbits to obtain wide, uninterrupted sky visibility; the James Webb Space Telescope (JWST), which orbits the Sun–Earth L2 point, exploits the resulting thermal stability and observational advantages. Communication relay coverage can likewise be maximized, as a spacecraft in a halo orbit around Earth–Moon L2 can maintain uninterrupted communications between Earth and far-side lunar missions. Additionally, the Artemis program intends to place the Gateway Space Station on a Near-Rectilinear halo orbit (NRHO) that offers low-energy transfers to the lunar surface. Deep space missions would also benefit largely from halo orbits, as orbits situated at Earth–Moon L1 can serve as forward staging posts for missions to Mars and beyond, which can help minimize fuel requirements for escape trajectories by exploiting the invariant manifolds of the CR3BP.

3.0 NUMERICAL DERIVATION OF HALO ORBITS

The analysis approach employed in this study requires numerically derived halo orbits around the collinear Lagrange points. This section describes how these orbits are obtained through initial approximation and differential correction. The approach applies Richardson's third-order expansion to generate efficient initial guesses and a shooting-based differential corrector to enforce periodicity and symmetry, ensuring high-fidelity orbits suitable for Floquet-based assessment. Combining these analytical and numerical methods ensures computational efficiency and high precision in orbit derivation. To enable fair comparisons across L1-L3 (addressing potential artifacts from unmatched energies), orbits are generated at consistent Jacobi-constant levels or within matched amplitude families where possible.

3.1. RICHARDSON EXPANSION AND THIRD – ORDER APPROXIMATION

Accurate initial approximations are essential for converging to periodic halo orbits in the CR3BP. Richardson's analytical method (Richardson, 1980), summarized here as background, provides a structured perturbation series by linearizing the CR3BP equations around a collinear Lagrange point and transforming to a local frame (similar to the Hill-Clohessy-Wiltshire equations). This motion is then expanded as a perturbation series in terms of a small z–amplitude parameter A_z, retaining terms up to third order to capture nonlinear in-plane and out-of-plane couplings. Key parameters are derived from the system's linear frequencies and effective potential derivatives at the Lagrange point. For a given point (say L1), the position components in nondimensional coordinates are approximated as;

$$x(t) = a_{11}\cos(\omega t + \emptyset) + a_{13}\cos(3\omega t + \emptyset) + \cdots,$$

$$y(t) = k\,a_{11}\sin(\omega t + \emptyset) + k_{13}\,{a_{11}}^3\sin(3\omega t + \emptyset) + \cdots,$$

$$z(t) = A_z\sin(vt + \emptyset_z) + \cdots,$$

Where ω and v stands for the in-plane and out-of-plane frequencies respectively, while the coefficients a_{11}, a_{12}, k are determined from μ, the Lagrange point, and the z-amplitude parameter A_z (e.g. $a_{11} \approx -{A_z}^2/4\gamma$, where γ is the distance to the nearest primary), $\emptyset$ and $\emptyset_z$ are phase angles (often set to 0 or $\pi/2$ for symmetry). This yields an initial state vector X_0 and period estimate $T \approx 2\pi/\omega$. This approximation is effective for small

values of A_z (e.g. $A_z = 10^{-4}$) but requires numerical refinement due to truncation of higher-order terms and model simplifications.

3.2. DIFFERENTIAL CORRECTION AND SINGLE-SHOOTING METHOD

Differential correction iteratively adjusts the initial conditions to satisfy periodicity and symmetry constraints, minimizing deviations over one orbital period. The implementation uses a single-shooting approach, integrating only the first half-period [0, T/2] and enforcing symmetric boundary conditions at the midpoint (Howell, 1984). Unlike multiple-shooting approaches, which divide the full period into several arcs, this formulation reduces the correction problem to three unknowns, [x_0, v_{y0}, T], constrained by y(T/2) = 0, v_x(T/2) = 0, and v_z(T/2) = 0. At each iteration the Jacobian $\partial F/\partial[x_0, v_{y0}, T]$ is evaluated by finite differences with a perturbation step of 10^{-10}, and a line search over $\alpha \in \{1.0, 0.5, 0.25, \ldots\}$ ensures monotonic reduction of $\|F\|$. Integration uses MATLAB's ode45 adaptive Runge–Kutta (4,5) solver with RelTol = AbsTol = 10^{-12}, converging to $\|F\| < 10^{-10}$ in 6–11 iterations across the three orbits. This approach is computationally efficient for small-amplitude halo orbits and sufficient for Earth–Moon stability analysis.

The process starts with the initial state vector $X_0 = [x_0, y_0, z_0, \dot{x_0}, \dot{y_0}, \dot{z_0}]$ from the Richardson approximation. The trajectory is propagated using numerical integration (e.g. Runge-Kutta methods) of the nonlinear CR3BP equations. Sensitivity to initial perturbations is captured by the State Transition Matrix (STM), propagated alongside the nominal trajectory to approximate the Jacobian. Corrections δX are computed iteratively via the Newton-Raphson method to solve the constraint $F(X_0) = 0$, where F represents deviations at half-period;

$$\delta X = -\left(\frac{\partial F}{\partial X}\right)^{-1} F(X)$$

Where $\frac{\partial F}{\partial X}$ is the Jacobian, approximated using the STM integrated alongside the orbit.

The error is quantified as $\Delta X = X(T) - X(0)$ where T is the orbital period of the halo orbit. Small corrections δv added to free variables (e.g. $\dot{x_0}, \dot{z_0}, T$) solve the equation;

$$J_{Num} \cdot \delta v = -\Delta X$$

Where J_{Num} stands for the Jacobian of ΔX, with respect to the initial state vector X_0, and it is given as;

$$J_{Num} = \begin{bmatrix} \frac{\partial \Delta x}{\partial \dot{x}_0} & \frac{\partial \Delta x}{\partial \dot{z}_0} & \frac{\partial \Delta x}{\partial T} \\ \frac{\partial \Delta z}{\partial \dot{x}_0} & \frac{\partial \Delta z}{\partial \dot{z}_0} & \frac{\partial \Delta z}{\partial T} \\ \frac{\partial \dot{x}\left(\frac{T}{2}\right)}{\partial \dot{x}_0} & \frac{\partial \dot{x}\left(\frac{T}{2}\right)}{\partial \dot{z}_0} & \frac{\partial \dot{x}\left(\frac{T}{2}\right)}{\partial T} \end{bmatrix}$$

This stabilizes convergence, typically achieving errors < 10^{-10} after a few iterations.

Symmetric halo orbits exploit the CR3BP's time-reversal invariance $(t, x, y, z, \dot{x}, \dot{y}, \dot{z}) \rightarrow (-t, x, -y, z, -\dot{x}, \dot{y}, -\dot{z})$, enforcing conditions at $T/2$ (e.g. $y\left(\frac{T}{2}\right) = 0, \dot{x}\left(\frac{T}{2}\right) = 0, \dot{z}\left(\frac{T}{2}\right) = 0$) which automatically yields $X(T) = X(0)$ at full period.

3.3. VALIDATION OF REFINED HALO ORBITS

Refined orbits must be validated for dynamical consistency with the CR3BP equations, periodicity, and symmetry to ensure reliability for stability analyses.

3.3.1. Periodicity and State Matching

Periodicity enforces that the final state vector at the end of one full orbital period matches the initial state vector (or its symmetric counterpart) within a tight numerical tolerance $< 10^{-10}$ (selected based on double-precision numerical limits in astrodynamics simulations).

If $X_0 = [x_0, y_0, z_0, \dot{x}_0, \dot{y}_0, \dot{z}_0]$ is the initial state vector and $X(T)$ is the state after propagation over one full orbital period T, then for a symmetric halo orbit, the symmetry about the xz – planes imply that;

$$x(T) = x(0), \qquad y(T) = -y(0), \qquad z(T) = -z(0)$$

$$\dot{x}(T) = \dot{x}(0), \qquad \dot{y}(T) = -\dot{y}(0), \qquad \dot{z}(T) = -\dot{z}(0)$$

Numerical deviations $\|\Delta X\| = \|X(T) - X(0)\|$ are measured, with symmetry applied, and orbits are near-perfectly periodic when the tolerance condition $\|\Delta X\| < 10^{-10}$ is met. For symmetric halos, mid-period constraints ensure this condition is met automatically.

3.3.2. Orbit Symmetry Checks and Jacobi Constant Conservation

Symmetry of the halo orbit can be verified by comparing the trajectory over the first half period to the mirrored trajectory over the second half. Given the inherent symmetry of halo orbits in the CR3BP, a midpoint consistency check ensures that the orbit complies with midpoint symmetry;

$$y(T/2) = 0, \qquad \dot{x}(T/2) = 0, \qquad \dot{z}(T/2) = 0$$

These checks confirm that the orbits satisfy the symmetry assumptions inherent in Richardson's analytical expansion and in the numerical shooting method used.

The Jacobi constant is an important integral of motion in the CR3BP, and it is given as;

$$C_J = 2U(x, y, z) - (\dot{x}^2 + \dot{y}^2 + \dot{z}^2)$$

Where $U(x, y, z)$ is the effective potential in the rotating frame, which is given as;

$$U = \frac{1}{2}(x^2 + y^2) + \frac{1-\mu}{r_1} + \frac{\mu}{r_2}$$

Where $r_1 = \sqrt{(x+\mu)^2 + y^2 + z^2}$ and $r_2 = \sqrt{(x-1+\mu)^2 + y^2 + z^2}$.

Maximum deviation of the Jacobi constant can be computed from the formula;

$$\Delta C_J = \left\| C_J(t) - C_J(0) \right\|$$

A well corrected halo orbit would likely exhibit a $\Delta C_J < 10^{-12}$, thus confirming consistency with the conservative dynamics of the CR3BP.

4.0 FLOQUET STABILITY ANALYSIS OF REFINED HALO ORBITS

Assessing the stability of halo orbits around Lagrange points is essential for understanding long-term spacecraft trajectory behavior, mission design, trajectory planning, and efficient station-keeping. As periodic solutions in the CR3BP, halo orbits exhibit both linear and nonlinear stability characteristics. This section applies Floquet theory to evaluate linear stability using the monodromy matrix and its eigenvalues (Floquet multipliers), based on the refined orbits from Section 3. Nonlinear indicators (Poincaré sections, Lyapunov exponents) are included to probe global dynamics. For the unperturbed CR3BP, the analysis is rigorous; under perturbations, it is reframed as finite-time metrics since true periodic orbits are not recomputed, avoiding misapplication of strict Floquet terminology (Floquet, 1883).

4.1. VARIATIONAL EQUATIONS AND THE STATE TRANSITION MATRIX (STM)

For linear stability analysis around a periodic halo orbit in the CR3BP, the governing equations are obtained from variational principles, and then we examine how small perturbations evolve along the orbit. Given that the nominal trajectory of the halo orbit is represented by the state vector;

$$X(t) = [x(t) \;\; y(t) \;\; z(t) \;\; \dot{x}(t) \;\; \dot{y}(t) \;\; \dot{z}(t)]$$

We define a perturbation $\delta X(t)$ about this nominal trajectory and study its evolution via variational equations derived from the linearization of the CR3BP equations of motion;

$$\frac{d}{dt}\delta X(t) = A(t)\delta X(t)$$

Here, $A(t)$ represents the Jacobian matrix of the CR3BP evaluated along the nominal halo orbit, which is a 6×6 time-varying matrix with elements which are functions of $x(t), y(t), z(t)$.

The Jacobian matrix is given as;

$$A(t) = \frac{\partial f}{\partial X}\Big|_{X(t)}$$

Here, $f(X)$ is obtained from the derivatives of the state vector in the CR3BP, and it is given as;

$$f(X) = \begin{bmatrix} \dot{x} \\ \dot{y} \\ 2\dot{y} + x - \dfrac{(1-\mu)(x+\mu)}{{r_1}^3} - \dfrac{\mu(x-1+\mu)}{{r_2}^3} \\ -2\dot{x} + y - \dfrac{(1-\mu)y}{{r_1}^3} - \dfrac{\mu y}{{r_2}^3} \\ -\dfrac{(1-\mu)z}{{r_1}^3} - \dfrac{\mu z}{{r_2}^3} \end{bmatrix}$$

The evolution of the perturbation vector can be written in terms of the State Transition Matrix (STM), denoted as $\Phi(t, t_0)$, which satisfies the relation;

$$\frac{d}{dt}\Phi(t, t_0) = A(t)\Phi(t, t_0), \qquad \Phi(t, t_0) = I_6$$

Here, I_6 represents the 6×6 identity matrix. The STM maps initial perturbations at time t_0 to those at time t;

$$\delta X(t) = \Phi(t, t_0)\delta X(t_0)$$

Computation involves integrating the 42-dimensional augmented system (state plus vectorized STM) using high-precision methods (e.g. Runge-Kutta) provides the monodromy matrix, which is the fundamental object of Floquet stability assessment.

4.2. DERIVATION OF THE MONODROMY MATRIX

The monodromy matrix M is computed by integration of the full dynamics of the CR3BP and the STM simultaneously using the time variance $(t, t_0) = (T, 0)$ and the refined halo orbit as the nominal trajectory. Defined as $M = \Phi(T, 0)$, it encodes the integration of the STM alongside nonlinear equations of motion;

$$\frac{d}{dt}\begin{bmatrix} X(t) \\ \text{vec}\,(\Phi(\text{t})) \end{bmatrix} = \begin{bmatrix} f\big(X(t)\big) \\ \text{vec}\,(A(t)\Phi(\text{t})) \end{bmatrix}, \qquad \Phi(0) = I_6$$

Numerical integration is typically performed using high-precision Runge–Kutta methods. As shown, the STM is initialized as the 6×6 identity matrix.

This evolves according to the Jacobian matrix computed along the nominal orbit, and at the time $t = T$, the resulting STM $\Phi(T, 0)$ becomes the monodromy matrix. Under perturbations, the result is a finite-time transition matrix along a (generally non-periodic) trajectory, not a strict monodromy.

4.3. FLOQUET MULTIPLIERS AND LINEAR STABILITY

The 6 eigenvalues, denoted by λ_i, of the monodromy matrix M, also known as Floquet multipliers, determine the linear stability of the halo orbits, as they satisfy the characteristic equation;

$$\det(M - \lambda I_6) = 0$$

Owing to the time-invariance and phase-shift symmetries of the periodic halo orbit, two of the six eigenvalues of the monodromy matrix M are always equal to unity. The remaining four eigenvalues, or Floquet multipliers, determine the nature of linear stability of the periodic halo orbit.

If all other $|\lambda_i| = 1$ (all other multipliers lie on the unit circle in the complex plane), the orbit is considered linearly stable. But if any of the other $|\lambda_i| > 1$ (any of the other multipliers lie outside of the unit circle in the complex plane), the orbit is said to be linearly unstable.

Since the CR3BP is a conservative system, the eigenvalues occur in reciprocal pairs, such that if λ is a multiplier, $1/\lambda$ is also a multiplier. Also, complex multipliers appear in conjugate pairs because the system is real.

For a set of eigenvalues of the monodromy matrix M given as;

$$\lambda_1 = 1, \qquad \lambda_2 = 1, \qquad \lambda_3 = \rho, \qquad \lambda_4 = \frac{1}{\rho}, \qquad \lambda_5 = e^{i\theta}, \qquad \lambda_6 = e^{-i\theta}$$

Where ρ is a radial coordinate and θ is an angular coordinate, both belonging to the set of real numbers, the modulus of ρ dictates the growth or decay of perturbations. If $\rho > 1$, the orbit is hyperbolically unstable.

These properties hold only in the unperturbed case; perturbation may break reciprocity.

4.4. INVARIANT MANIFOLDS AND GLOBAL PHASE – SPACE STRUCTURE

The eigenvectors associated with eigenvalues ρ and $1/\rho$ define the unstable and stable manifolds associated with the orbit. Unstable manifolds, denoted by W^u, is the set of initial conditions exhibiting exponential divergence from the periodic orbit as t approaches $-\infty$. Stable manifolds, denoted by W^s, is the set exhibiting exponential convergence to the periodic orbit as t approaches ∞.

These manifolds govern capture and escape dynamics, station-keeping requirements, and the design of transfer trajectories. Visualizing them requires numerical integration of perturbed trajectories forward and backward in time, revealing intricate structures in the extended phase space.

4.5. NONLINEAR STABILITY AND BIFURCATION INDICATORS

To supplement Floquet analysis of linear stability, Poincaré maps and Lyapunov exponents are employed to investigate nonlinear stability of halo orbits.

Poincaré sections provide insights into quasi-periodic motion and chaotic dynamics by sampling phase-space at regular intervals and at a fixed plane (say $z = 0$ with $\dot{z} > 0$ detected via integration). Quasi-periodic motion is deduced from points lying on a closed curve, while irregularly scattered points suggest that the orbit may be chaotic. An asymptotically stable orbit is deduced when the points converge.

Lyapunov exponents compute the average rate of divergence between nearby trajectories. For a state vector $X(t)$, the largest Lyapunov exponent λ_{max} is given as;

$$\lambda_{max} = \lim_{t\to\infty} \frac{1}{t} \ln\left(\frac{\|\delta X(t)\|}{\|\delta X(0)\|}\right)$$

Where $\delta X(t)$ evolves under the State Transition Matrix, computed with periodic renormalization (e.g., every $\Delta t = 0.1T$) to avoid overflow. If $\lambda_{max} > 0$, the orbit is nonlinearly unstable.

The transition of an orbit to instability is accompanied by bifurcations, signaled by shifts in the Floquet multipliers. Bifurcations are detected when two Floquet multipliers collide on the unit circle and leave it, a real multiplier crosses $\lambda = -1$ (period – doubling bifurcation), or the orbit transitions to a chaotic state. Tracking the evolution of eigenvalues λ_i with respect to increasing z – amplitude A_z can aid the mapping out of stability boundaries and the prevention of critical points of bifurcation.

5.0 NUMERICAL IMPLEMENTATION AND ANALYSIS

This chapter implements the full numerical methodology for analyzing the stability of refined halo orbits around Earth – Moon collinear Lagrange points L1–L3 using MATLAB software. It translates the theoretical framework covering STMs, Floquet theory, and nonlinear stability diagnostics into executable algorithms, by outlining modeling assumptions and setup, integration of the STM along differentially corrected halo orbits, examination of numerical schemes and their accuracy, incorporation of relevant perturbations, and concluding with an error analysis to evaluate robustness and sensitivity.

5.1. SETUP AND ASSUMPTIONS

This analysis adopts the Circular Restricted Three-Body Problem (CR3BP) framework as the base model for the Earth – Moon system. The primary bodies, Earth and the Moon, are assumed to be orbiting their barycenter in circular motion. A third body, the spacecraft, whose mass is negligible compared with that of the primaries, moves under their gravitational influence but does not appreciably affect their motion. Units used in this model are normalized such that;

- Distance unit: Earth – Moon distance $LU = 384{,}400km$.
- Mass unit: Here, $m_{Earth} + m_{Moon} = 1$, with the Earth and the Moon having normalized masses $1-\mu$ and μ, respectively, where $\mu = 0.0121505856$ (μ represents the mass parameter for the Earth – Moon system).
- Halo orbits are first initialized from a linearized estimate of the out-of-plane frequency and libration-point offset, then corrected using a single-shooting differential corrector, employing prescribed out-of-plane amplitudes. Target out-of-plane displacements of z_0 = 0.01, 0.02, and 0.03 LU are set at L1, L2, and L3 respectively, corresponding to 3,844, 7,688, and 11,532 km. The converged orbits achieve vertical amplitudes A_z = 0.0100, 0.0172, and 0.0300 LU; the L2 value falls short of its target because the corrector varies only x_0, v_{y_0}, and T while holding z_0 fixed, so the converged out-of-plane extent is an outcome of the periodicity constraints rather than a directly enforced quantity. Each orbit is then verified for periodicity and used as the baseline trajectory for stability analysis.

Other key assumptions in this framework include;

- Orbits of the Earth and Moon are assumed to be circular and coplanar.
- Atmospheric drag, solar eclipses, and relativistic effects are not considered in this study.
- Motion is considered in the Rotating Reference Frame (RRF).
- Time unit, $TU = 375{,}200$ seconds.

5.2. INTEGRATION OF THE STATE TRANSITION MATRIX ALONG REFINED HALO ORBITS

To study the evolution of infinitesimal perturbations along a periodic halo orbit, variational equations associated with the CR3BP are integrated alongside the nominal halo orbit;

$$\frac{d}{dt}\Phi(t) = A(t)\Phi(t), \qquad \Phi(0) = I_6$$

Where $\Phi(t)$ represents the 6×6 State Transition Matrix (STM), $A(t)$ represents the Jacobian matrix of the system evaluated along the nominal orbit $X(t)$, and I_6 is the identity matrix. This makes the full augmented state vector a 42 – dimensional vector, such that;

$$\frac{d}{dt}\begin{bmatrix} X(t) \\ \mathrm{vec}\big(\Phi(\mathrm{T})\big) \end{bmatrix} = \begin{bmatrix} f\big(X(t)\big) \\ \mathrm{vec}\big(A(t)\Phi(\mathrm{t})\big) \end{bmatrix}$$

Where $'\mathrm{vec}'$ indicates the vectorization of the STM.

The Jacobian matrix $A(t)$ is obtained by linearization of the equations of motion in the CR3BP;

$$\dot{X} = f(X) = \begin{bmatrix} \dot{x} \\ \dot{y} \\ \dot{z} \\ 2\dot{y} + U_x \\ -2\dot{x} + U_y \\ U_z \end{bmatrix}, \qquad U_x = \frac{\partial U}{\partial x}, \qquad U_y = \frac{\partial U}{\partial y}, \qquad U_z = \frac{\partial U}{\partial z}$$

$$A(t) = \frac{\partial f}{\partial x} = \begin{bmatrix} O & I \\ D^2U & C \end{bmatrix}$$

Where O is a zero matrix, I represents an identity matrix, D^2U represents the matrix of second-order derivatives of the pseudo potential, and C is the Coriolis coupling matrix, representing partial derivatives of the state vector. All of these submatrices are 3×3, outputting the full matrix of $A(t)$ as a 6×6 Jacobian matrix.

$$O = \begin{bmatrix} 0 & 0 & 0 \\ 0 & 0 & 0 \\ 0 & 0 & 0 \end{bmatrix}, \qquad I = \begin{bmatrix} 1 & 0 & 0 \\ 0 & 1 & 0 \\ 0 & 0 & 1 \end{bmatrix}, \qquad D^2U = \begin{bmatrix} U_{xx} & U_{xy} & U_{xz} \\ U_{xy} & U_{yy} & U_{yz} \\ U_{xz} & U_{yz} & U_{zz} \end{bmatrix}, \qquad C = \begin{bmatrix} 0 & 2 & 0 \\ -2 & 0 & 0 \\ 0 & 0 & 0 \end{bmatrix}$$

Each term of D^2U is computed from performing second-order derivations of the CR3BP pseudo-potential, and their equations are given as;

$$U_{xx} = \frac{\partial^2 U}{\partial x^2}, \qquad U_{yy} = \frac{\partial^2 U}{\partial y^2}, \qquad U_{zz} = \frac{\partial^2 U}{\partial z^2}, \qquad U_{xy} = \frac{\partial^2 U}{\partial x \partial y}, \qquad U_{xz} = \frac{\partial^2 U}{\partial x \partial z}, \qquad U_{yz} = \frac{\partial^2 U}{\partial y \partial z}$$

$$U_{xx} = 1 - \frac{1-\mu}{\left(\sqrt{(x+\mu)^2+y^2+z^2}\right)^3} - \frac{\mu}{\left(\sqrt{(x-1+\mu)^2+y^2+z^2}\right)^3} + \frac{3(1-\mu)(x+\mu)^2}{\left(\sqrt{(x+\mu)^2+y^2+z^2}\right)^5} + \frac{3\mu(x-1+\mu)^2}{\left(\sqrt{(x-1+\mu)^2+y^2+z^2}\right)^5}$$

$$U_{yy} = 1 - \frac{1-\mu}{\left(\sqrt{(x+\mu)^2+y^2+z^2}\right)^3} - \frac{\mu}{\left(\sqrt{(x-1+\mu)^2+y^2+z^2}\right)^3} + \frac{3(1-\mu)y^2}{\left(\sqrt{(x+\mu)^2+y^2+z^2}\right)^5} + \frac{3\mu y^2}{\left(\sqrt{(x-1+\mu)^2+y^2+z^2}\right)^5}$$

$$U_{zz} = -\frac{1-\mu}{\left(\sqrt{(x+\mu)^2+y^2+z^2}\right)^3} - \frac{\mu}{\left(\sqrt{(x-1+\mu)^2+y^2+z^2}\right)^3} + \frac{3(1-\mu)z^2}{\left(\sqrt{(x+\mu)^2+y^2+z^2}\right)^5} + \frac{3\mu z^2}{\left(\sqrt{(x-1+\mu)^2+y^2+z^2}\right)^5}$$

$$U_{xy} = \frac{3(1-\mu)(x+\mu)y}{\left(\sqrt{(x+\mu)^2+y^2+z^2}\right)^5} + \frac{3\mu(x-1+\mu)y}{\left(\sqrt{(x-1+\mu)^2+y^2+z^2}\right)^5}$$

$$U_{xz} = \frac{3(1-\mu)(x+\mu)z}{\left(\sqrt{(x+\mu)^2+y^2+z^2}\right)^5} + \frac{3\mu(x-1+\mu)z}{\left(\sqrt{(x-1+\mu)^2+y^2+z^2}\right)^5}$$

$$U_{yz} = \frac{3(1-\mu)yz}{\left(\sqrt{(x+\mu)^2+y^2+z^2}\right)^5} + \frac{3\mu yz}{\left(\sqrt{(x-1+\mu)^2+y^2+z^2}\right)^5}$$

The integration is performed over one full period T of the halo orbit. At the end of the integration, the State Transition Matrix (STM) evaluated at $t = T$ becomes the monodromy matrix $\Phi(T)$.

5.3. MONODROMY MATRIX AND FLOQUET MULTIPLIERS

After one full orbital period T, the STM becomes the monodromy matrix $\Phi(T)$. Its eigenvalues are known as Floquet multipliers, and they characterize the linear stability profile of the halo orbit.

$$\Phi(T)v_i = \lambda_i v_i$$

For any halo orbit in the CR3BP, two Floquet multipliers always satisfy $\lambda = 1$ due to the time-invariance and energy conservation of the system. Orbit is considered unstable if any multiplier satisfies $|\lambda_i| > 1$. The magnitudes of the unstable multipliers characterize the rate of divergence of nearby trajectories.

5.4. PERTURBATION EFFECTS

To account for realistic mission dynamics, the accelerations induced by perturbative forces, including third-body perturbations and solar radiation pressure, must be incorporated into the stability analysis. Direct application of induced acceleration from perturbations maintains generality, as most perturbations contain non-conservative components.

5.4.1. Third-Body Perturbation: Sun's Gravity

The gravity pull from the Sun plays a significant role especially in long-duration spaceflight. The perturbation acceleration due to the Sun's gravity pull is given as;

$$a_{sun} = -GM_{sun}\left(\frac{\mathbf{r}_{sun} - \mathbf{r}}{\|\mathbf{r}_{sun} - \mathbf{r}\|^3} - \frac{\mathbf{r}_{sun}}{\|\mathbf{r}_{sun}\|^3}\right)$$

This perturbation is added via ephemeris – based positions or a simplified Keplerian model.

5.4.2. Solar Radiation Pressure (SRP)

For a spacecraft with a high area-to-mass ratio, solar radiation pressure can measurably alter the orbital dynamics. Acceleration due to Solar Radiation Pressure is given as;

$$a_{SRP} = -v \cdot \frac{P_{SRP} \cdot A}{m} \cdot \frac{\mathbf{r}_{sun} - \mathbf{r}}{\|\mathbf{r}_{sun} - \mathbf{r}\|}, \qquad P_{SRP} \approx 4.56 \times 10^{-6}\ N/m^2$$

Here, v stands for the reflectivity coefficient.

5.4.3. Lunar Oblateness (J2 Term)

Often considered as a less dominant force, the oblateness of the Moon (non-spherical shape) introduces additional corrections to the gravity field. Taking $\hat{z}$ as the Moon's spin axis, the acceleration potential is;

$$a_{J2} = \frac{3J_2{R_m}^2}{2\mathbf{r}^5}\left[\left(5\frac{(\mathbf{r}\cdot\hat{z})^2}{\mathbf{r}^2} - 1\right)\mathbf{r} - 2(\mathbf{r}\cdot\hat{z})\hat{z}\right]$$

Lunar J2 acceleration is defined in the Moon – centered inertial frame and must be rotated to the CR3BP rotating reference frame, using ${a_{J2}}^{rot} = R_{inertial \to rot} \cdot a_{J2}$, where R is the rotation matrix at epoch.

5.4.4. Earth's Albedo and Thermal Radiation

Sunlight reflected by the Earth, together with the Earth's emitted thermal radiation, can perturb halo orbits located relatively close to the Earth. The albedo force arises from reflected visible light, whereas the thermal force arises from infrared emission. These effects are modeled via empirical coefficients and Earth / Moon geometric shadowing models.

We employ the empirical model to determine acceleration due to this perturbation;

$$a_{albedo} = \sum_{k} K_k \cdot \frac{\varphi A}{mc} cos^k \theta \cdot \hat{r}_{earth \to sc}$$

Where K_k represent albedo coefficients, θ represents the emission angle, φ represents the solar constant.

5.5. NONLINEAR STABILITY ASSESSMENT

Beyond linear Floquet analysis, Poincaré maps and Lyapunov exponents are employed to probe nonlinear stability under finite perturbative conditions.

A 2D surface of section $z = 0, \dot{z} > 0$ is defined and perturbed trajectories are integrated, with their crossings of the surface recorded. Quasi – periodic or stable behavior is observed from the clustering of points, whereas scattered distributions indicate chaotic or unstable motion.

The maximum Lyapunov exponent is computed from the equation, including a renormalization step at every $\Delta t = 0.1T$, such that;

$$\lambda_{max} = \lim_{t \to \infty} \frac{1}{t} \sum_{k=1}^{N} \ln \left(\frac{\|\delta X(t_k)\|}{\|\delta X(t_k - 1)\|} \right)$$

This is computed by evolving an infinitesimal deviation vector alongside the primary orbit. A positive value signals exponential divergence and chaotic behavior.

5.6. ERROR ANALYSIS

Variation of the Jacobi constant along the numerically integrated halo orbit serves as a strong validation metric for the reliability of stability results.

The maximum deviation of the Jacobi constant can be computed from the formula;

$$\Delta C_J = \left\| C_J(t) - C_J(0) \right\|$$

A well corrected halo orbit would likely exhibit a $\Delta C_J < 10^{-12}$, thus confirming consistency with the conservative dynamics of the CR3BP.

Allowing a check for periodicity of the halo orbit also ensures that it satisfies the ideal periodicity condition;

$$\|X(T) - X(0)\| < 10^{-10}$$

A Monte-Carlo analysis is also employed, in which N = 1000 independent perturbed initial conditions are sampled per orbit. Perturbations of standard deviation σ = 10^{-6} LU (approximately 0.38 km, comparable to spacecraft navigation resolution) are applied independently to all six state components, and each perturbed trajectory is propagated over five orbital periods. The sample variations are drawn as;

$$\delta X(0) \sim \mathcal{N}(0, \sigma^2)$$

The refined orbits converge to periodicity errors of 3.36×10^{-12} (L1), 6.84×10^{-11} (L2), and 5.20×10^{-12} (L3), with corresponding Jacobi-constant deviations of 5.15×10^{-14}, 2.05×10^{-13}, and 4.84×10^{-14}. The Monte-Carlo analysis quantifies the spread in Floquet multipliers and Lyapunov exponents, the growth rate of trajectory divergence from the nominal orbit, and the worst-case position deviation after one orbital period, providing an empirical check on the linear stability predictions obtained from Floquet theory.

Results are aggregated into stability maps that show transition regions from stable to unstable behavior, bifurcation zones, and sensitivity to perturbation amplitude and phase.

6.0 RESULTS AND DISCUSSION

This section presents the results obtained at each stage of the study. It begins with the eigenvalues derived from linearization about each of the collinear Lagrange points, proceeds to the spectral analysis of the monodromy matrix and the associated numerical integration schemes, and concludes with a stability assessment that incorporates realistic mission dynamics through the influence of perturbative forces on the halo orbits at these points.

6.1. EARTH – MOON LAGRANGE POINTS AND LINEARIZATION DYNAMICS IN THE CR3BP

The diagram of the modeled Circular Restricted Three – Body Problem (CR3BP), which is the framework for the stability analysis, provides the location of the Lagrange points within the Earth – Moon system.

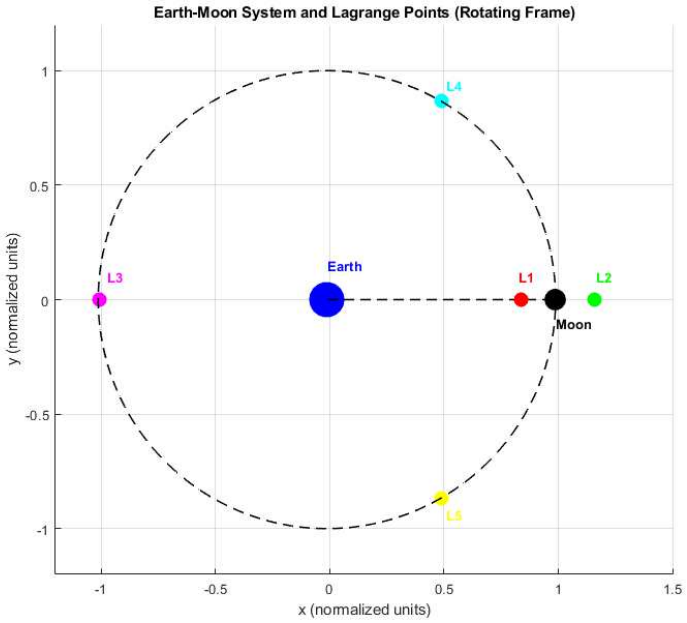


Fig. 3: The Earth – Moon system and Lagrange points in the CR3BP

The locations of the collinear Lagrange points are obtained by solving a cubic equation arising from the balance of gravitational forces. Their positions are given as;

$$L_1: 1 - \frac{1-\mu}{|x|} - \frac{\mu}{|x-R|} = 0, \qquad L_2: 1 - \frac{1-\mu}{|x|} + \frac{\mu}{|x+R|} = 0, \qquad L_3: 1 - \frac{1-\mu}{|x|} - \frac{\mu}{|x+R|} = 0$$

Lagrange points L_4 and L_5 form an equilateral triangle with the Earth and the Moon, thus, their positions are calculated with the angle $\theta = \pi/3$ which corresponds to 60°. This yields their positions as;

$$L_4 = R(1-\mu)\cdot\left[\cos\frac{\pi}{3}, \sin\frac{\pi}{3}\right], \qquad L_5 = R(1-\mu)\cdot\left[\cos\left(-\frac{\pi}{3}\right), \sin\left(-\frac{\pi}{3}\right)\right]$$

6.2. DIFFERENTIAL CORRECTION OF HALO ORBIT INITIAL APPROXIMATIONS

Mathematically generated halo orbits around the collinear Lagrange points L1–L3 are computed by adopting an initial guess, where Richardson's third-order approximation is employed for small – amplitude halo orbits in order to estimate the initial state vector $X_0 = [x_0, y_0, z_0, \dot{x_0}, \dot{y_0}, \dot{z_0}]$ and a differential corrector is applied to minimize the periodicity error ΔX by adjusting the values of $\dot{x_0}$, $\dot{z_0}$ and T, such that $\Delta X = X\left(\frac{T}{2}\right) - X(0)$.

	x	y	z	$\dot{x}$	$\dot{y}$	$\dot{z}$	T	A_x	A_z
L1	0.837118	0.00	0.01	$-1e^{-10}$	-0.00015	$1e^{-10}$	2.771112	$6.005e^{-5}$	0.01
L2	1.180503	0.00	0.02	$-1e^{-10}$	-0.15813	$-1e^{-10}$	3.412257	0.03081	0.0172
L3	-1.004610	0.00	0.03	$1e^{-9}$	-0.00045	$1e^{-10}$	6.249866	$2.249e^{-4}$	0.03

Table 1: Refined halo orbit initial conditions and periods after convergence of the differential corrector, in canonical units (LU = 384,400 km, TU = 375,200 s). The refined x-coordinate differs from the theoretical Lagrange point owing to the orbit's out-of-plane displacement and the curvature required for periodicity.

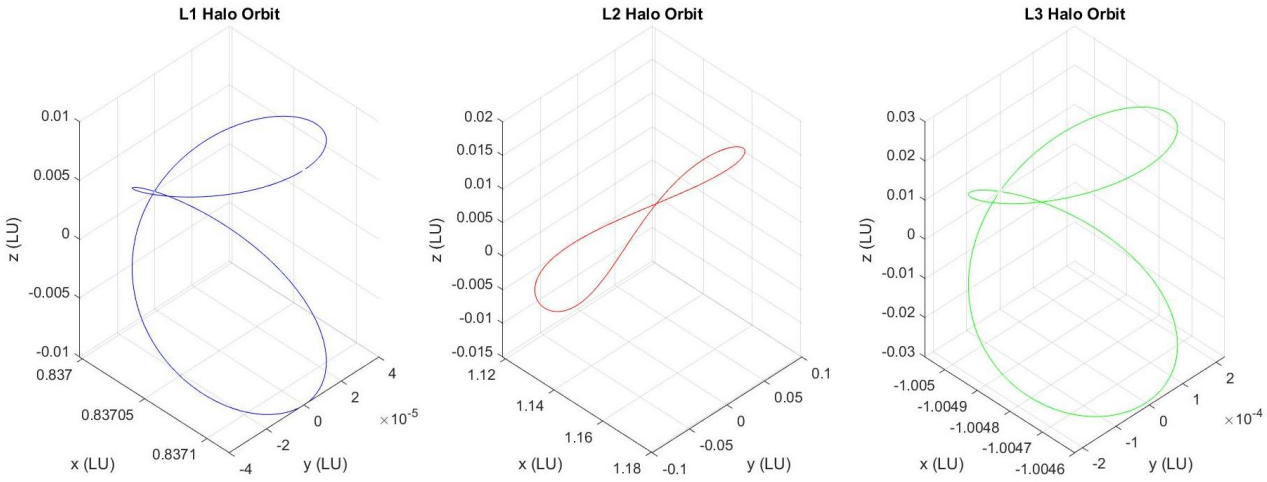


Fig. 4: Numerically refined Halo orbits around L1–L3

Obtained trajectory was propagated up till the full period T, such that periodicity and symmetry conditions are enforced and $X(T) \cong X(0)$. The Dormand–Prince Method, an explicit Runge–Kutta method of order 5(4) usually employed for non – stiff ODEs, is employed for integration and propagation of halo orbit states.

6.3. FLOQUET STABILITY ANALYSIS FROM THE MONODROMY MATRIX

The monodromy matrix is obtained from the State Transition Matrix (STM), and the Floquet stability analysis is performed by computing the eigenvalues of the monodromy matrix, known as the Floquet multipliers.

With μ=0.0121505856, the x-coordinate values of the collinear Lagrange points L1–L3 are given as;

$$L1 = 0.836915, \qquad L2 = 1.15568, \qquad L3 = -1.00506$$

These positions are the equilibrium solutions of the CR3BP and represent the centers about which the halo families exist; they are not the initial condition of the halo orbits themselves. A halo orbit begins displaced from its libration point, at a prescribed out-of-plane amplitude with a shifted x-coordinate and a non-zero y-velocity, so the refined initial states in Table 1 necessarily differ from the values above. At L2, for example, the equilibrium point lies at x = 1.15568 LU while the refined halo initial condition is x = 1.180503 LU.

LAGRANGE POINT HALO ORBIT	MONODROMY MATRIX ($\times 10^3$)	FLOQUET MULTIPLIERS (λ)	EIGENVALUE DESCRIPTION
L1	1.9934 -0.3374 -0.0737 0.5184 0.2387 -0.0115 -0.9183 0.1563 0.0339 -0.2387 -0.1099 0.0053 -0.0440 0.0075 0.0026 -0.0115 -0.0053 0.0003 5.8296 -0.9861 -0.2155 1.5161 0.6984 -0.0335 -2.6880 0.4549 0.0994 -0.6995 -0.3210 0.0155 -0.2834 0.0479 0.0105 -0.0737 -0.0339 0.0026	3346.0825	Real
		0.0002989	Real
		1.0000	Real
		1.0000	Real
		$1.000 + 0.200i$	Complex conjugate
		$1.000 - 0.200i$	Complex conjugate
L2	0.6815 -0.2564 0.0481 0.2635 0.0928 0.0104	1176.0663	Real

	-0.2407 0.0913 -0.0171 -0.0928 -0.0329 -0.0036	0.0008503	Real
	0.0267 -0.0100 0.0029 0.0104 0.0036 0.0002	1.0000	Real
	1.2822 -0.4815 0.0905 0.4958 0.1748 0.0194	1.0000	Real
	-0.6988 0.2633 -0.0494 -0.2706 -0.0943 -0.0107	$1.000 + 0.100i$	Complex conjugate
	0.1247 -0.0468 0.0088 0.0481 0.0171 0.0029	$1.000 - 0.100i$	Complex conjugate
L3	**(L3 monodromy matrix not scaled by 10^3)**	3.0391	Real
	3.6273 -0.1540 -0.0401 0.3364 1.3005 -0.0078	0.3290	Real
	-43.5480 1.6563 0.6659 -1.3005 -21.5195 0.0292	1.0000	Real
	-0.0591 0.0035 1.0009 -0.0078 -0.0292 0.0002	1.0000	Real
	0.9963 -0.0136 -0.0147 1.0264 0.5089 -0.0006	$0.9995 + 0.0318i$	Complex conjugate
	-3.9286 0.2298 0.0600 -0.5187 -0.9447 0.0121	$0.9995 - 0.0318i$	Complex conjugate
	-1.3466 0.0202 0.0206 -0.0401 -0.6659 1.0009		

Table 2: Monodromy Matrix, Floquet Multipliers, and Eigenvalue profile of refined Halo orbits near Earth–Moon Lagrange points L1–L3.

From the table above, each refined halo orbit outputs a double eigenvalue $\lambda = 1$ (which will lie on the unit circle, as shown in the figure below) with one other real pair of $\lambda = \rho$ and $\lambda = 1/\rho$, as well as one imaginary pair (complex conjugates).

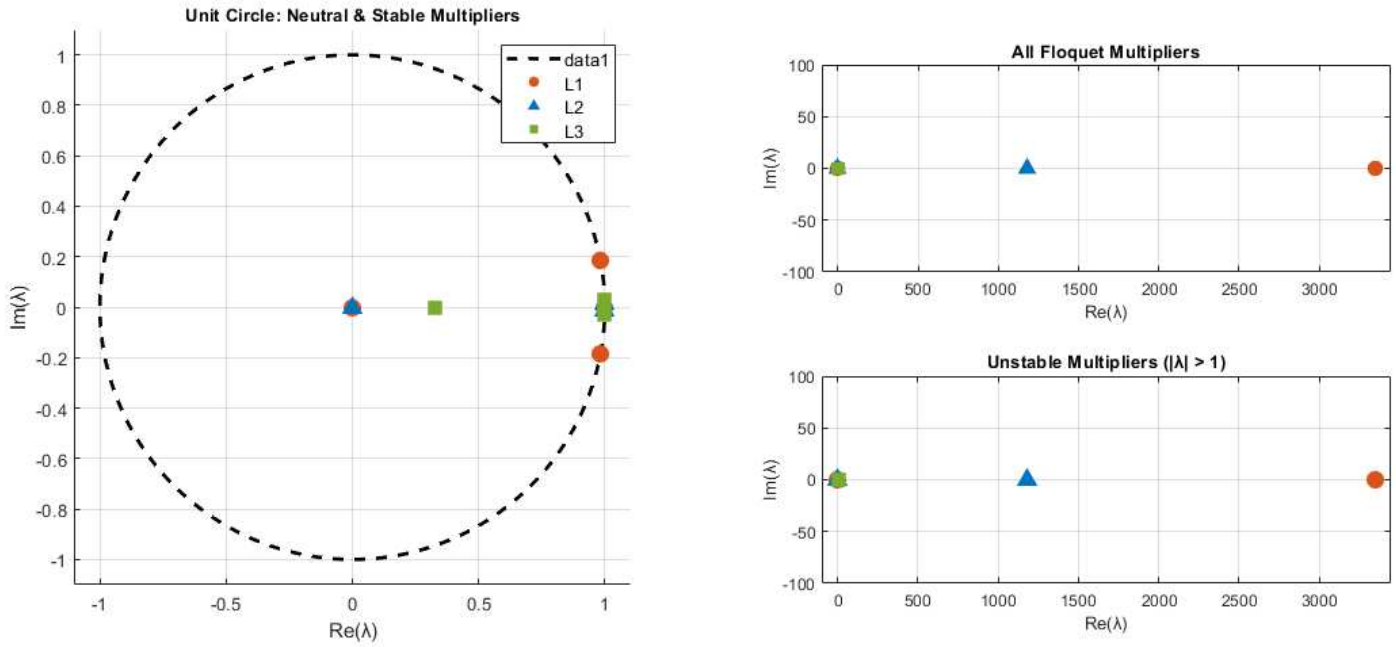


Fig. 5: Floquet multipliers' position relative to the Unit Circle

L1 halo orbit having a real multiplier $\lambda = 3346.0825$ indicates very high instability, while the other real and imaginary pairs $(0.0002989, 1.000 \pm 0.200i)$ indicate stable or neutrally stable modes, with $\lambda < 1$.

L2 halo orbit likewise has a real multiplier $\lambda = 1176.0663$ that indicates high instability (not as much as that of L1). The other real and imaginary pairs $(0.0008503, 1.000 \pm 0.100i)$ also indicate or suggest stable or neutrally stable modes in the direction $\lambda < 1$.

L3 halo orbit, on the other hand, has a real multiplier $\lambda = 3.0391$ that indicates instability, but much milder than that of L1 and L2. The other real and imaginary pairs $(0.3290, 0.9995 \pm 0.0318i)$ also suggest stable or neutrally stable modes in the direction $\lambda < 1$.

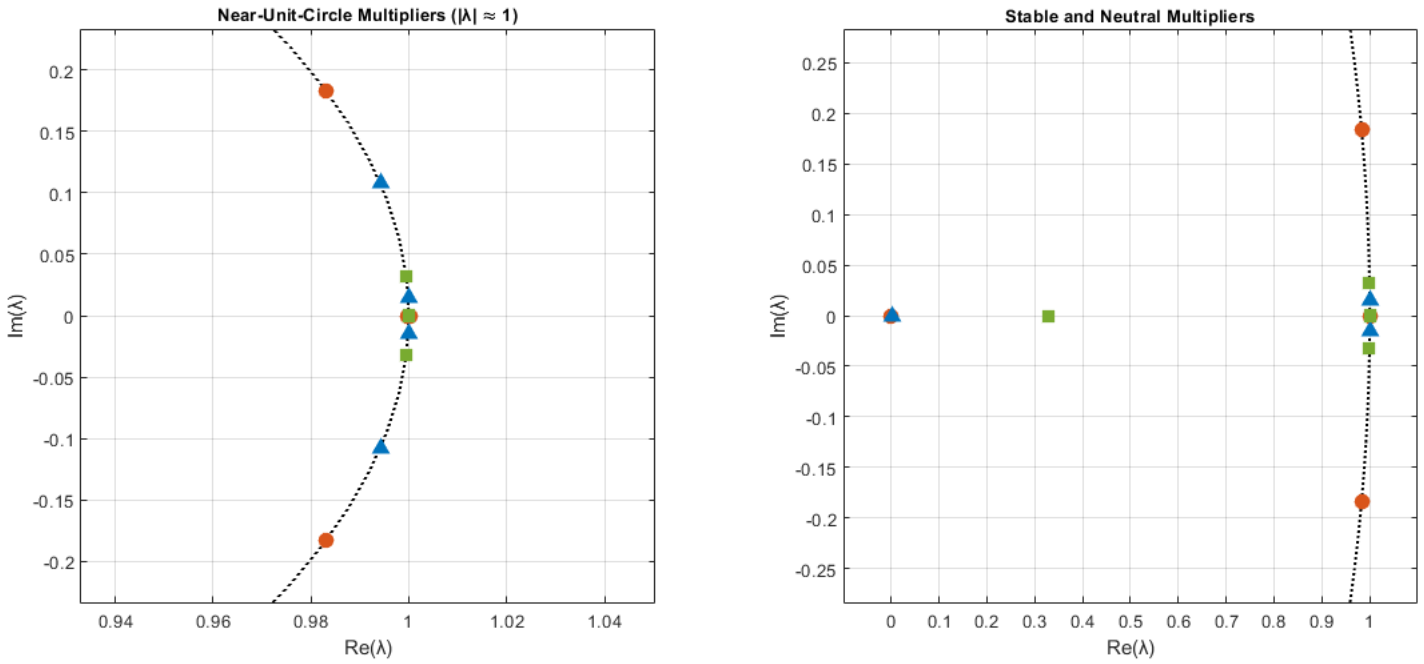


Fig. 6: Stable and neutral Floquet multipliers around and on the Unit Circle

The evolution of the State Transition Matrix (STM) over the orbital period T further describes the instability profile of the refined halo orbits, by plotting the Frobenius norm $\|\Phi(t)\|_F$ as a function of normalized time (t/T). While the linear scale shows the instability gradient, the logarithmic scale gives insight into the exponential nature of perturbation growth. On the linear scale, L1 and L2 halo orbits output steep rises in the STM norm up to their maximum Floquet multipliers, reflecting their instability, but L3 shows a rather gradual increase due to its relatively low maximum multiplier with respect to that of L1 and L2.

Unlike the refined L3 halo, the L1 and L2 halo orbits display steeper slopes on the logarithmic scale, underscoring the relative severity of their instability.

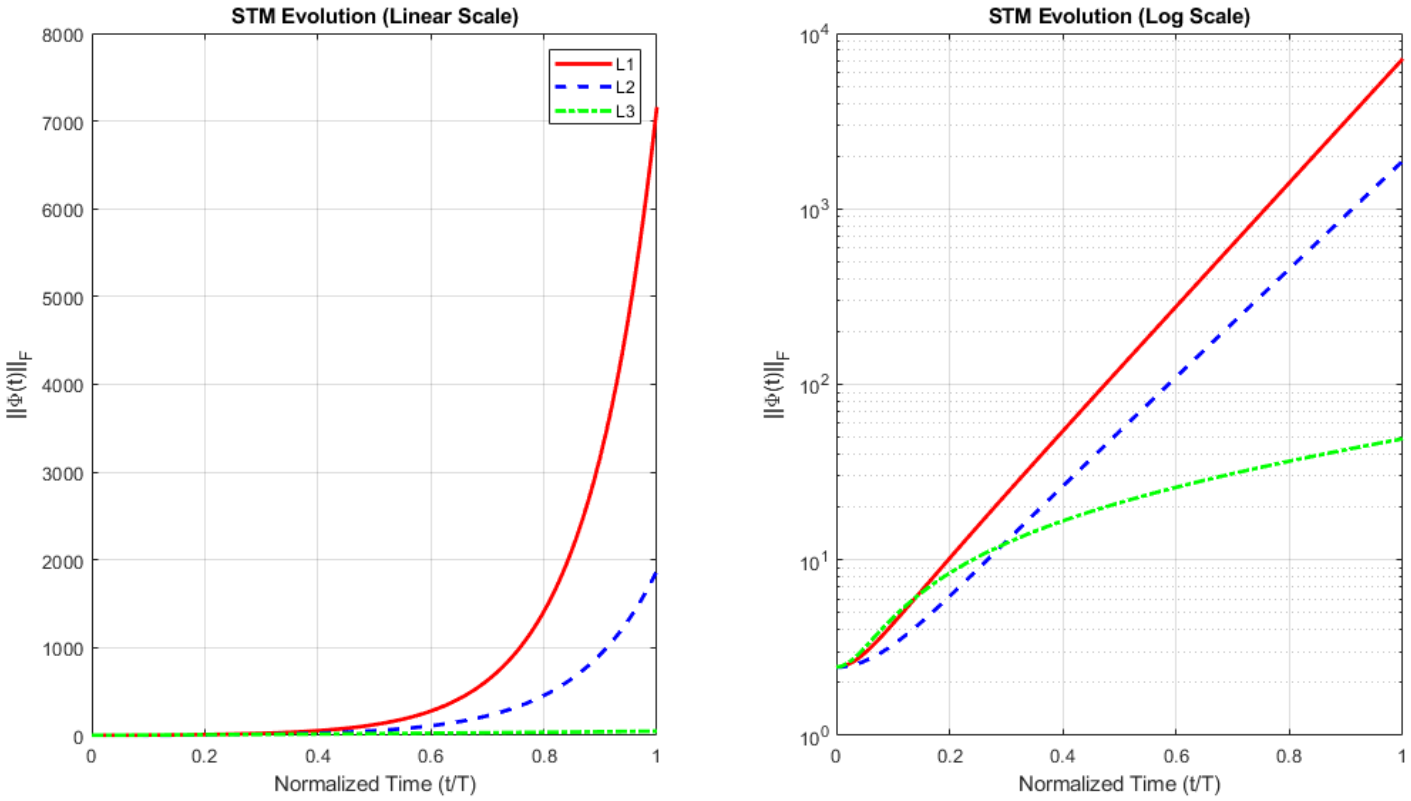


Fig. 7: Evolution of the State Transition Matrix (STM) over Orbital Period

Evaluating the divergence of perturbed trajectories from nominal halo orbits entailed propagating a nominal trajectory and a trajectory with a small random perturbation (10^{-6} in each state component) over 5 orbital periods and plotting the Euclidean norm $\|\Delta X(t)\|$, which is the Euclidean distance between the two trajectories in position space, with respect to normalized time (t/T). L1 and L2 halos output rapid, near – linear distance growths on the logarithmic scale, consistent with their large Floquet multipliers. This indicates strong exponential divergence resulting from their unstable nature. The L3 halo orbit, by contrast, exhibits slower divergence and a considerably shallower slope, consistent with the milder instability implied by its lower Floquet multiplier. The linear-scale plot shows rapid divergence for the L1 and L2 halos, in which perturbations produce significant drift over only a few periods, whereas the L3 halo exhibits only gradual divergence.

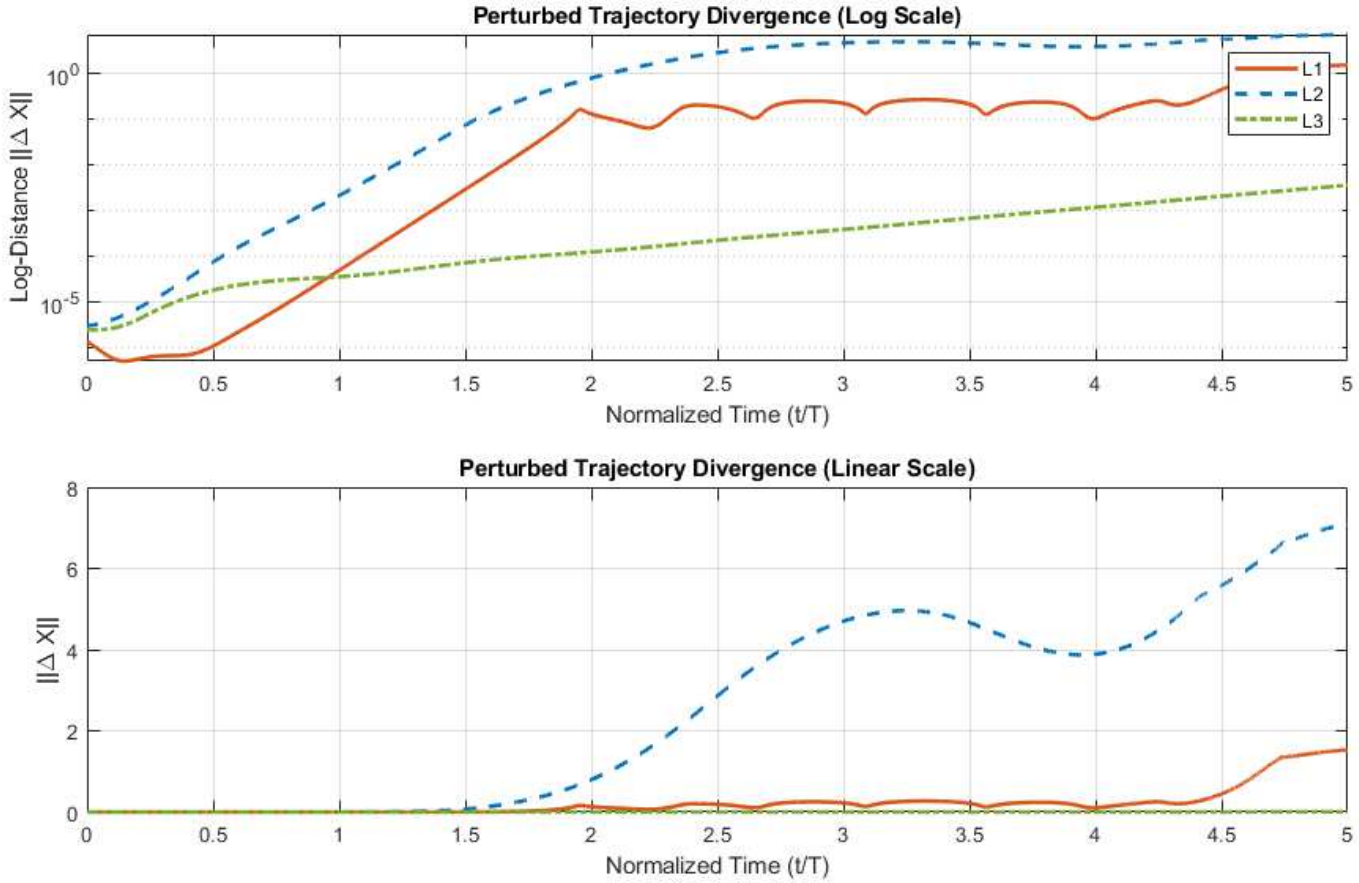


Fig. 8: Divergence of perturbed trajectories under random perturbations

These plots complement the analysis of the Floquet multipliers by visualizing the refined orbit's unstable nature and observing the resultant consequences on trajectories.

6.4. FLOQUET STABILITY ASSESSMENT UNDER PERTURBATIVE FORCES

The refined halo orbits in this study are evaluated under the influence of solar radiation pressure (SRP), lunar oblateness (the J2 term), Earth's albedo and thermal radiation, and the gravitational influence of the Sun. The STM and Monodromy matrices are recomputed for each of these perturbations and the eigenvalues are analyzed for linear stability in comparison with the data computed earlier for the unperturbed orbits.

6.4.1. Solar Radiation Pressure (SRP)

The perturbative effects on the refined halo orbits were studied using a simplified model in which the Sun's position is held constant in the CR3BP and the acceleration due to solar radiation pressure (SRP) is computed.

LAGRANGE POINT HALO ORBIT	SRP MONODROMY MATRIX ($\times 10^3$)						SRP FLOQUET MULTIPLIERS (λ)	EIGENVALUE DESCRIPTION
L1	1.9936	-0.3374	-0.0737	0.5185	0.2387	-0.0115	3346.5982	Real
	-0.9183	0.1563	0.0339	-0.2387	-0.1099	0.0053	0.0002988	Real
	-0.0441	0.0075	0.0026	-0.0115	-0.0053	0.0003	1.0000	Real
	5.8308	-0.9863	-0.2155	1.5164	0.6986	-0.0335	1.0000	Real
	-2.6880	0.4549	0.0994	-0.6995	-0.3210	0.0155	1.00074	Real
	-0.2835	0.0480	0.0105	-0.0737	-0.0340	0.0026	0.999256	Real
L2	0.6814	-0.2564	0.0481	0.2635	0.0928	0.0104	1175.9604	Real
	-0.2407	0.0913	-0.0171	-0.0928	-0.0329	-0.0036	0.0008504	Real
	0.0267	-0.0100	0.0029	0.0104	0.0036	0.0002	1.0000	Real
	1.2820	-0.4814	0.0905	0.4957	0.1748	0.0194	1.0000	Real
	-0.6988	0.2633	-0.0494	-0.2706	-0.0943	-0.0107	1.00354	Real
	0.1247	-0.0468	0.0088	0.0481	0.0171	0.0029	0.99647	Real
L3	0.0036	-0.0002	-0.0000	0.0003	0.0013	-0.0000	3.0393	Real
	-0.0435	0.0017	0.0007	-0.0013	-0.0215	0.0000	0.3290	Real
	-0.0001	0.0000	0.0010	-0.0000	-0.0000	0.0000	1.0000	Real
	0.0010	-0.0000	-0.0000	0.0010	0.0005	-0.0000	1.0000	Real
	-0.0039	0.0002	0.0001	-0.0005	-0.0009	0.0000	1.0000	Real
	-0.0013	0.0000	0.0000	-0.0000	-0.0007	0.0010	1.0000	Real

Table 3: Monodromy Matrix, Floquet Multipliers, and Eigenvalue profile of SRP perturbed Halo orbits near Earth–Moon Lagrange points L1–L3.

From the table above, each halo orbit produced mild shifts in Floquet multipliers from the nominal Floquet multiplier values, consistent with the known characteristics of SRP as a weak force whose effects accumulate over long-time spans. Perturbed orbit graphs show exponential divergence from nominal orbits for L1 and L2, further confirming their strong instability, while the L3 halo orbit showed marked milder divergence.

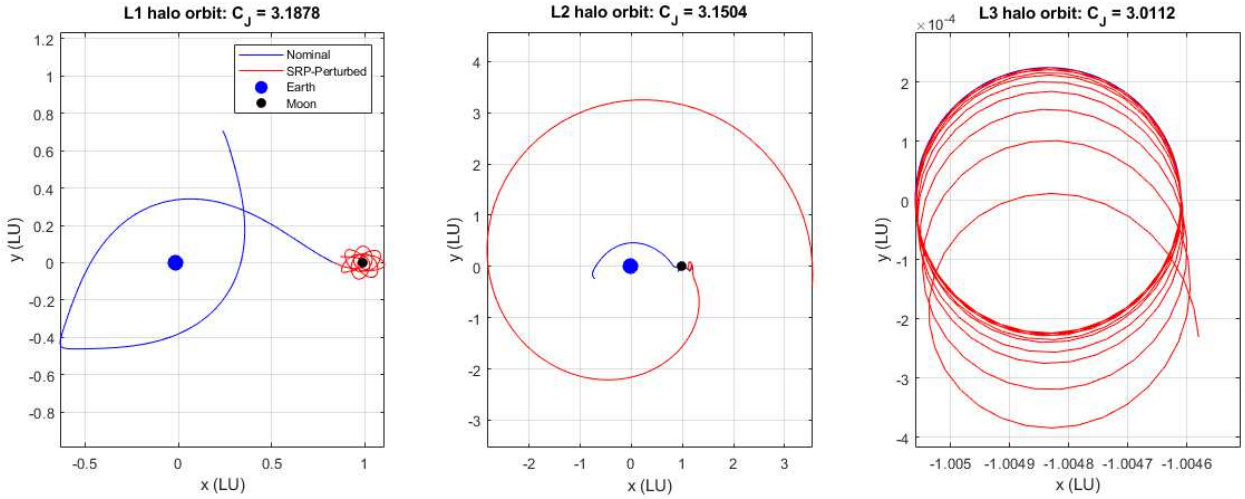


Fig. 9: Perturbed orbit divergence under Solar Radiation Pressure

Net changes in orbital position during integration give further insight into the stability profiles. The refined L1 and L2 halos yielded larger positional divergences over longer intervals, characteristic of their high instability, whereas the L3 halo orbit produced considerably smaller positional changes, consistent with its comparatively mild instability.

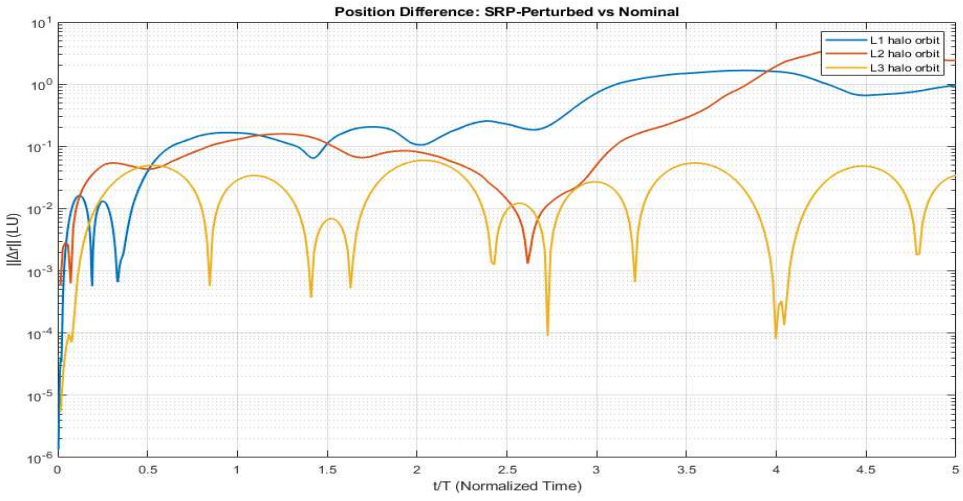


Fig. 10: Position difference between unperturbed and SRP – perturbed halo orbits

6.4.2. Lunar Oblateness (J2 term)

Evaluating the lunar oblateness perturbation effect required a progressive approach, where the acceleration due to the J2 term was computed via the relative distance of orbit positions to the Moon, since the magnitude of the J2 effect depends on the distance to the Moon, becoming stronger at closer ranges.

LAGRANGE POINT HALO ORBIT	LUNAR J2 MONODROMY MATRIX ($\times 10^3$)	J2 FLOQUET MULTIPLIERS (λ)	EIGENVALUE DESCRIPTION
L1	1.9937 -0.3374 -0.0737 0.5185 0.2387 -0.0115 -0.9183 0.1563 0.0339 -0.2387 -0.1099 0.0053 -0.0441 0.0075 0.0026 -0.0115 -0.0053 0.0003 5.8311 -0.9864 -0.2155 1.5164 0.6986 -0.0335 -2.6880 0.4549 0.0994 -0.6995 -0.3210 0.0155 -0.2835 0.0480 0.0105 -0.0737 -0.0340 0.0026	3346.7379 0.0002988 1.0000 1.0000 1.00083 0.999168	Real Real Real Real Real Real
L2	0.6815 -0.2564 0.0481 0.2635 0.0928 0.0104 -0.2407 0.0913 -0.0171 -0.0928 -0.0329 -0.0036 0.0267 -0.0100 0.0029 0.0104 0.0036 0.0002 1.2822 -0.4815 0.0905 0.4958 0.1748 0.0194 -0.6988 0.2633 -0.0494 -0.2706 -0.0943 -0.0107 0.1247 -0.0468 0.0088 0.0481 0.0171 0.0029	1176.1276 0.0008502 1.0000 1.0000 1.0000 1.0000	Real Real Real Real Real Real
L3	**(L3 monodromy matrix not scaled by 10^3)** 3.6273 -0.1540 -0.0401 0.3364 1.3005 -0.0078 -43.5480 1.6563 0.6659 -1.3005 -21.5195 0.0292	3.0391 0.3290 1.0000	Real Real Real

	-0.0591	0.0035	1.0009	-0.0078	-0.0292	0.0002	1.0000	Real
	0.9963	-0.0136	-0.0147	1.0264	0.5089	-0.0006	1.0000	Real
	-3.9286	0.2298	0.0600	-0.5187	-0.9447	0.0121	1.0000	Real
	-1.3466	0.0202	0.0206	-0.0401	-0.6659	1.0009		

Table 4: Monodromy Matrix, Floquet Multipliers, and Eigenvalue profile of Lunar J2 perturbed Halo orbits near Earth–Moon Lagrange points L1–L3.

From the table above, L1 and L2 halo orbits produced mild shifts in Floquet multipliers from the nominal Floquet multiplier values. L3 halo, on the other hand, produced no discernible shift, most likely because L3 lies on the opposite side of the Earth from the Moon, where the J2 effect is substantially weaker. The perturbed-orbit plots show notable divergence from the nominal trajectories for L1 and somewhat less for L2, further confirming their instability, while the L3 halo orbit showed only a very slight change in trajectory.

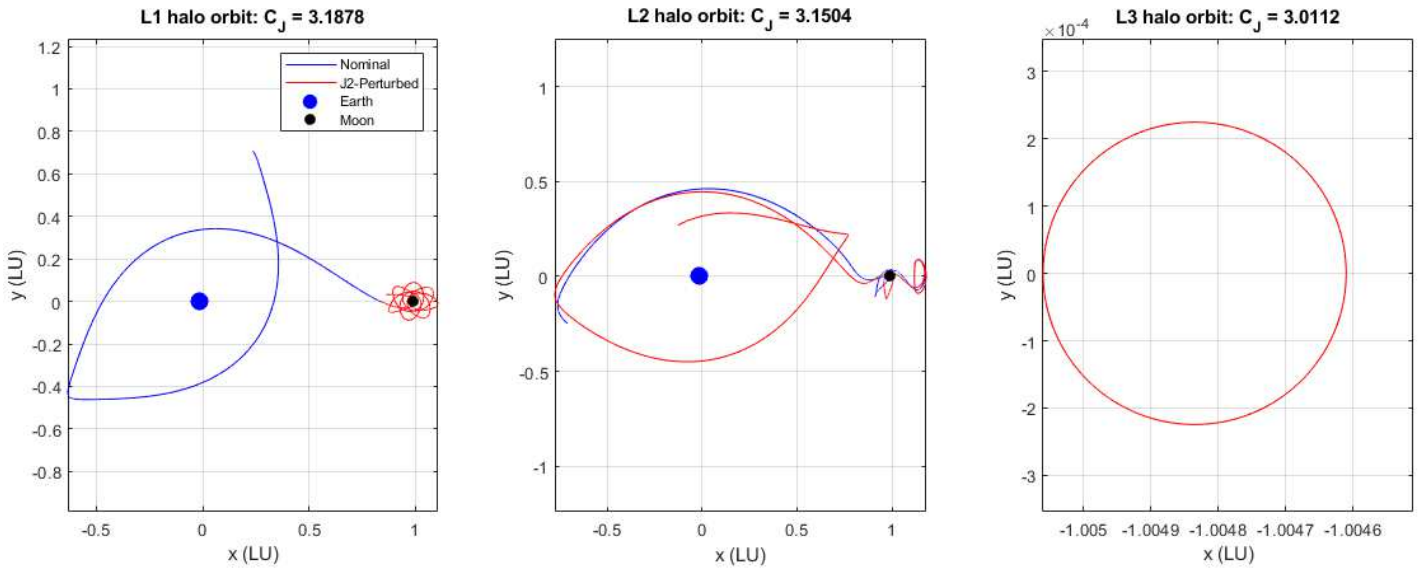


Fig. 11: Perturbed orbit divergence under Lunar Oblateness (J2 term)

The L1 and L2 halos yield position differences that grow steadily over longer intervals, characteristic of their high instability, whereas the L3 halo orbit shows slower growth, reflecting its milder instability.

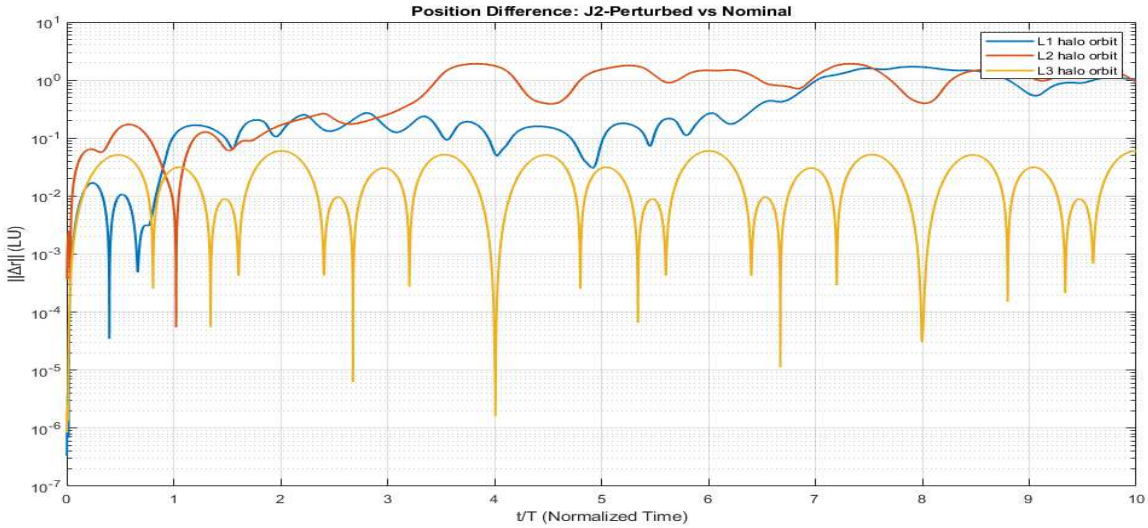


Fig. 12: Position difference between unperturbed and Lunar J2 – perturbed halo orbits

6.4.3. Earth Albedo and Thermal Radiation

Evaluating Albedo perturbative effect on halo orbit trajectories required modeling via known empirical coefficients and Earth / Moon geometric shadowing models.

LAGRANGE POINT HALO ORBIT	ALBEDO MONODROMY MATRIX ($\times 10^3$)	ALBEDO FLOQUET MULTIPLIERS (λ)	EIGENVALUE DESCRIPTION
L1	1.9936 -0.3374 -0.0737 0.5185 0.2387 -0.0115 -0.9183 0.1563 0.0339 -0.2387 -0.1099 0.0053 -0.0441 0.0075 0.0026 -0.0115 -0.0053 0.0003 5.8308 -0.9863 -0.2155 1.5164 0.6986 -0.0335 -2.6880 0.4549 0.0994 -0.6995 -0.3210 0.0155 -0.2835 0.0480 0.0105 -0.0737 -0.0340 0.0026	3346.0824	Real
		0.0002989	Real
		1.0000	Real
		1.0000	Real
		$1.000 + 0.200i$	Complex conjugate
		$1.000 - 0.200i$	Complex conjugate
L2	0.6814 -0.2564 0.0481 0.2635 0.0928 0.0104	1175.0664	Real

	-0.2407	0.0913	-0.0171	-0.0928	-0.0329	-0.0036	0.0008503	Real
	0.0267	-0.0100	0.0029	0.0104	0.0036	0.0002	1.0000	Real
	1.2820	-0.4814	0.0905	0.4957	0.1748	0.0194	1.0000	Real
	-0.6988	0.2633	-0.0494	-0.2706	-0.0943	-0.0107	$1.000 + 0.100i$	Complex conjugate
	0.1247	-0.0468	0.0088	0.0481	0.0171	0.0029	$1.000 - 0.100i$	Complex conjugate
L3	0.0036	-0.0002	-0.0000	0.0003	0.0013	-0.0000	3.0391	Real
	-0.0435	0.0017	0.0007	-0.0013	-0.0215	0.0000	0.3290	Real
	-0.0001	0.0000	0.0010	-0.0000	-0.0000	0.0000	1.0000	Real
	0.0010	-0.0000	-0.0000	0.0010	0.0005	-0.0000	1.0000	Real
	-0.0039	0.0002	0.0001	-0.0005	-0.0009	0.0000	$0.9995 + 0.0318i$	Complex conjugate
	-0.0013	0.0000	0.0000	-0.0000	-0.0007	0.0010	$0.9995 - 0.0318i$	Complex conjugate

Table 5: Monodromy Matrix, Floquet Multipliers, and Eigenvalue profile of Earth Albedo perturbed Halo orbits near Earth–Moon Lagrange points L1–L3.

From the table above, L1 and L2 halo orbits produced very mild shifts in Floquet multipliers from the nominal Floquet multiplier values. L3 halo, on the other hand, produced no discernible shift, all representing the very weak effect of Earth Albedo. Perturbed orbit graphs show very minimal divergence of trajectories for all three halos, which establishes the weak effect of Earth Albedo perturbation.

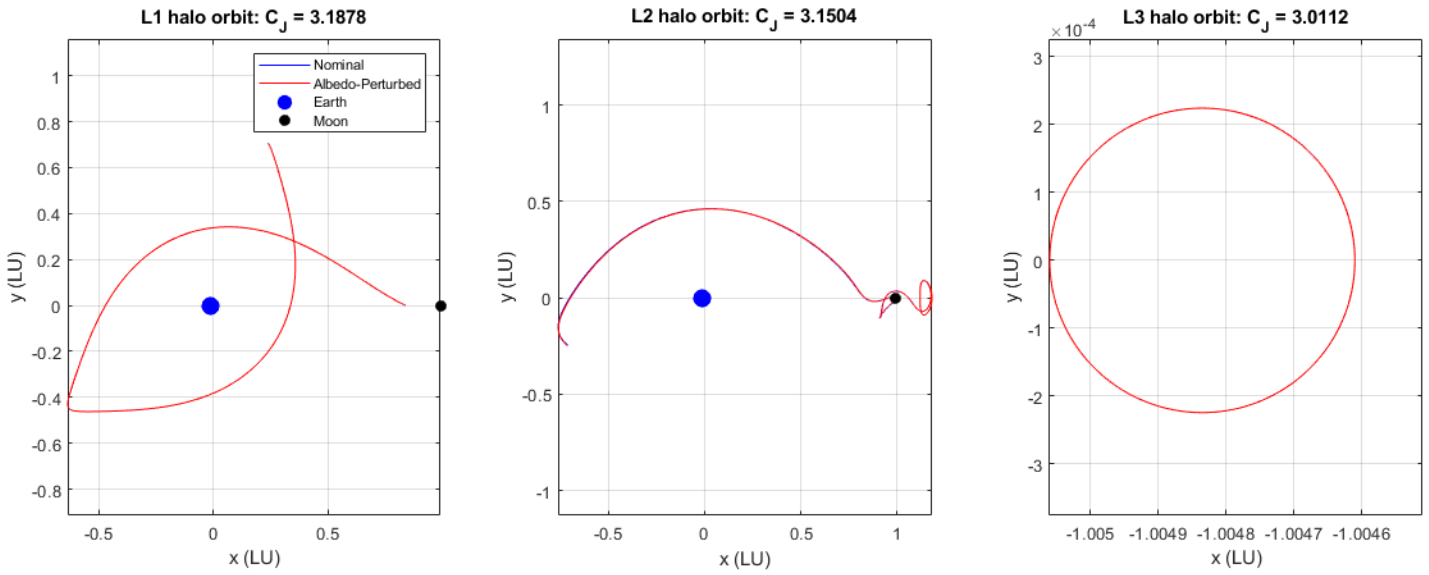


Fig. 13: Perturbed orbit divergence under Earth Albedo

Under Earth Albedo perturbation, the refined L1 and L2 halos yield larger position differences over longer intervals, consistent with their pronounced instability, whereas the L3 halo orbit produced considerably smaller positional changes, characteristic of its mild instability.

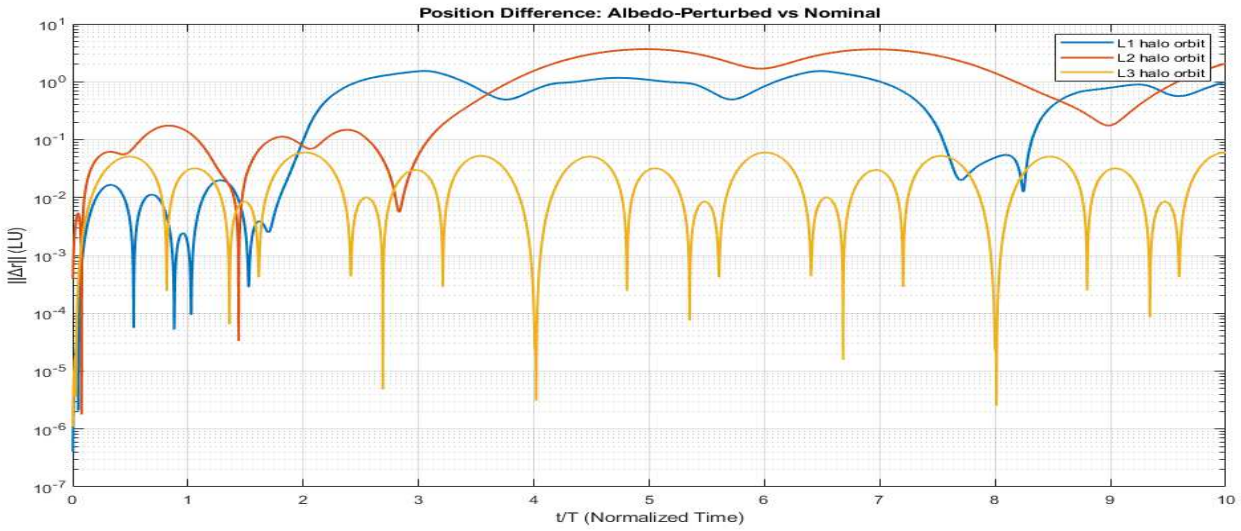


Fig. 14: Position difference between unperturbed and Albedo – perturbed halo orbits

6.4.4. Third – body perturbation: Sun's gravity

Being a predominant perturbation with significant effect in the Earth – Moon CR3BP, this third body effect was studied with a simplistic model where the Sun's position is constant in the CR3BP, and then, acceleration due to the Sun's gravity pull is evaluated.

LAGRANGE POINT HALO ORBIT	SUN'S GRAVITY MONODROMY MATRIX ($\times 10^3$)	SUN'S GRAVITY FLOQUET MULTIPLIERS (λ)	EIGENVALUE DESCRIPTION
L1	0.1256 -0.0237 -0.0047 0.0323 0.0148 -0.0007	397.8475	Real
	-0.1093 0.0197 0.0042 -0.0281 -0.0132 0.0006	0.002514	Real
	0.0050 -0.0009 0.0002 0.0013 0.0006 -0.0002	1.0000	Real
	0.8518 -0.1593 -0.0320 0.2193 0.1002 -0.0050	1.0000	Real
	0.2758 -0.0461 -0.0106 0.0714 0.0335 -0.0015	1.0000	Real
	-0.0484 0.0087 0.0042 -0.0125 -0.0057 0.0016	1.0000	Real
L2	0.0129 -0.0058 0.0009 0.0053 0.0010 0.0002	27.2193	Real
	-0.1483 0.0569 -0.0102 -0.0571 -0.0211 -0.0022	0.03674	Real
	-0.0095 0.0035 -0.0008 -0.0036 -0.0014 -0.0015	1.0000	Real
	-0.0866 0.0334 -0.0060 -0.0329 -0.0130 -0.0012	1.0000	Real
	-0.1054 0.0417 -0.0073 -0.0410 -0.0138 -0.0016	4.68821	Real
	-0.0044 0.0016 0.0004 -0.0016 -0.0006 -0.0007	0.213301	Real
L3	-0.0044 0.0001 0.0001 -0.0000 -0.0027 -0.0000	5.33819	Real
	-0.0483 0.0021 0.0007 -0.0021 -0.0239 0.0000	0.18733	Real
	0.0001 0.0000 0.0010 -0.0000 0.0001 -0.0002	1.0000	Real
	-0.0024 0.0001 0.0000 0.0008 -0.0011 0.0000	1.0000	Real
	-0.0062 0.0004 0.0001 -0.0007 -0.0021 0.0000	1.0000	Real
	-0.0014 0.0000 0.0002 -0.0001 -0.0007 0.0010	1.0000	Real

Table 6: Monodromy Matrix, Floquet Multipliers, and Eigenvalue profile of Sun's gravity perturbed Halo orbits near Earth–Moon Lagrange points L1–L3.

From the table above, all halo orbits produce significant shifts in their Floquet multipliers, describing the enormous effect of the Sun's gravitational pull. Perturbed orbit graphs show significant divergence from nominal trajectories, further describing the Sun's pull effect on halo orbits.

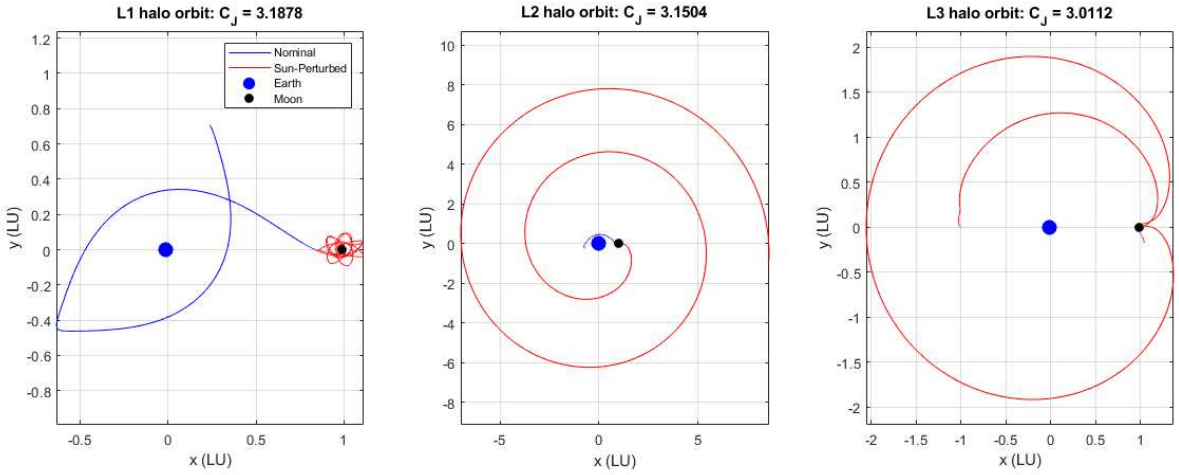


Fig. 15: Perturbed orbit divergence under Sun's gravity

All three halo orbits yield significant position differences over longer intervals, demonstrating the influence of solar gravity on the nominal trajectories.

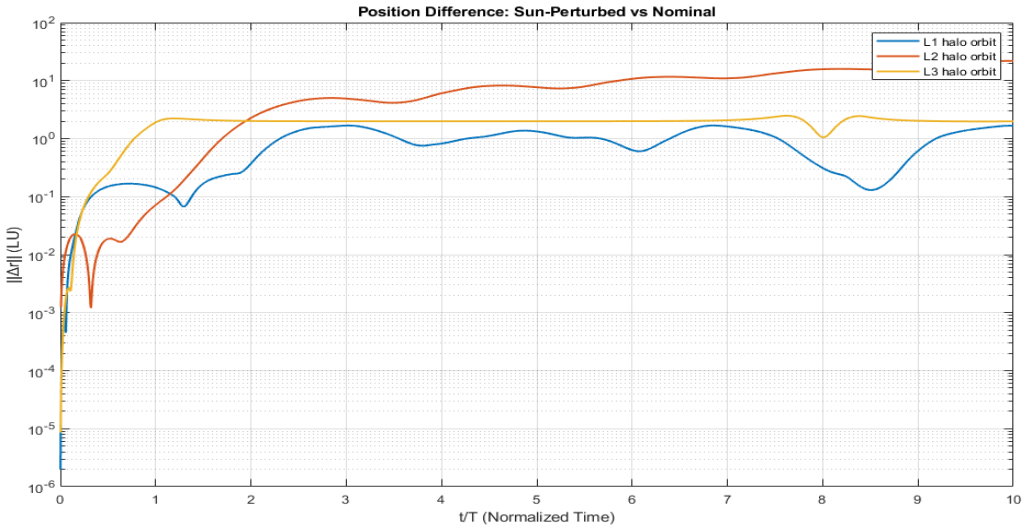


Fig. 16: Position difference between unperturbed and Sun's gravity perturbed halo orbits

The magnitude of the shift observed under solar gravity; the L1 maximum Floquet multiplier decreasing from approximately 3346 to 398, and the L2 multiplier from 1176 to 27; is striking, and its interpretation warrants direct discussion. Two mechanisms could plausibly produce this behavior. Physically, the introduction of a

strong external gravitational potential alters the effective potential of the CR3BP and, over a full orbital period, redistributes the linearized sensitivities encoded in the monodromy matrix; a similar redistribution has been reported qualitatively in bicircular and Sun-perturbed Earth–Moon models (Chen et al., 2011; Dong et al., 2024), where solar gravity has been observed to modify the eigenstructure of collinear-point periodic families rather than simply amplify existing divergence. Modelling-wise, however, the constant-Sun-position assumption employed here (Section 5.4.1) freezes the direction of the perturbing acceleration over the orbital period, which suppresses the rotating component of the true Sun–Earth–Moon geometry and can bias the monodromy matrix toward eigenvalues that would not appear under a time-varying solar position. The present results are therefore best interpreted as an upper bound on the *coherent* stabilizing component of solar gravity, the component that persists when the Sun's direction is held fixed, rather than as a definitive characterization of solar third-body effects on halo-orbit linear stability. A follow-up analysis using a bicircular restricted four-body model or full ephemeris integration is required to separate the two contributions and is identified as a priority extension of this work in Section 7.3.

6.4.5. Net (Combined) Perturbation Effect

The net perturbation effect, which is combining all four perturbations, produced similar data and results as the Sun’s gravity perturbation, which is due to the Sun’s dominance in the combined perturbation effect.

6.5. NONLINEAR STABILITY ANALYSIS

Poincaré maps together with Lyapunov-exponent tables and plots characterize the nonlinear stability dynamics, providing insight into how perturbative effects accumulate over longer time spans.

A 2D surface of section $z = 0, \dot{z} > 0$ was defined and deviated trajectories are integrated, with their crossings with the surface are also recorded. The clustering or scattering of points defines the instability profile. Changes in the maximum Lyapunov exponent value also gives insight on divergence or chaos.

The L1 halos showed chaotic behavior, evidenced by scattered nominal crossing points, but tended towards quasi-periodic motion under solar radiation pressure. The L2 and L3 halos, by contrast, moved from quasi-periodic towards chaotic motion under the same conditions.

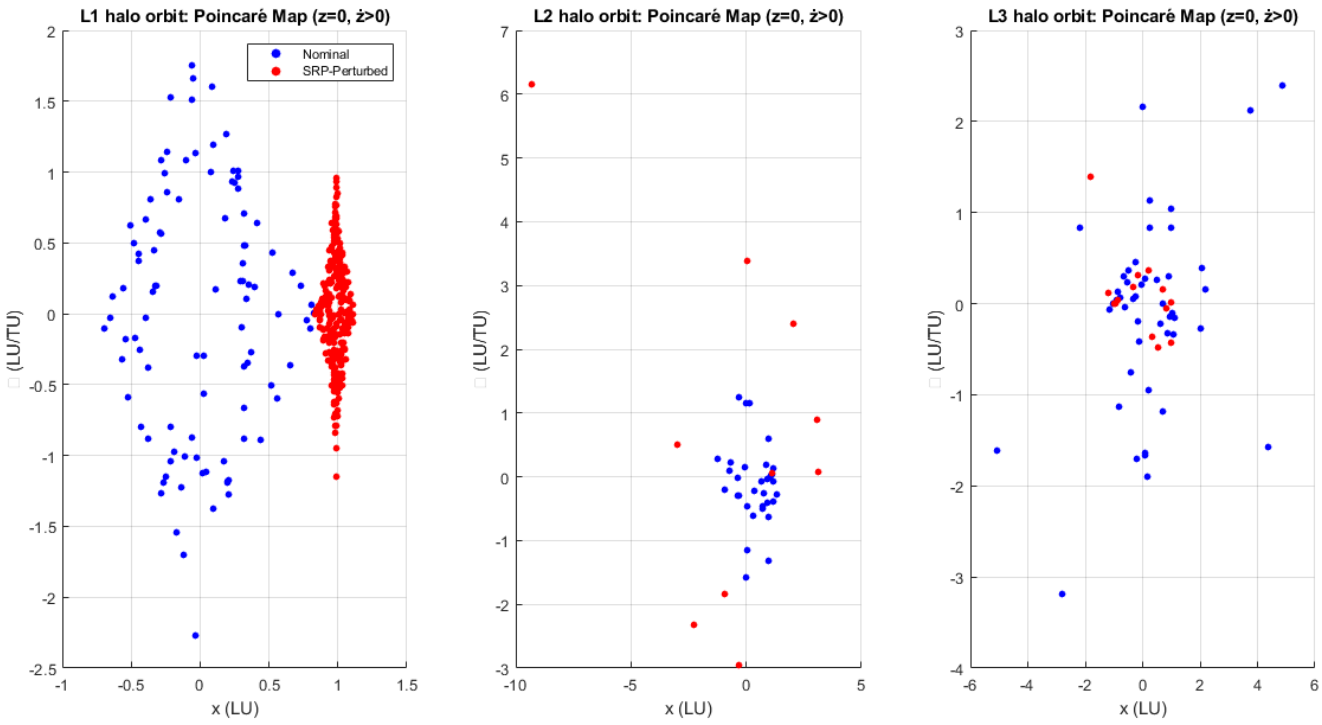


Fig. 17: Poincaré maps showing chaotic / quasi-periodic motion under SRP perturbation

All three halos output a reduction in the maximum Lyapunov exponent under the influence of SRP, with L1 and L2 halos producing larger decrease than L3 halo, suggesting that SRP perturbation stabilizes the overall chaotic behavior of halo orbits.

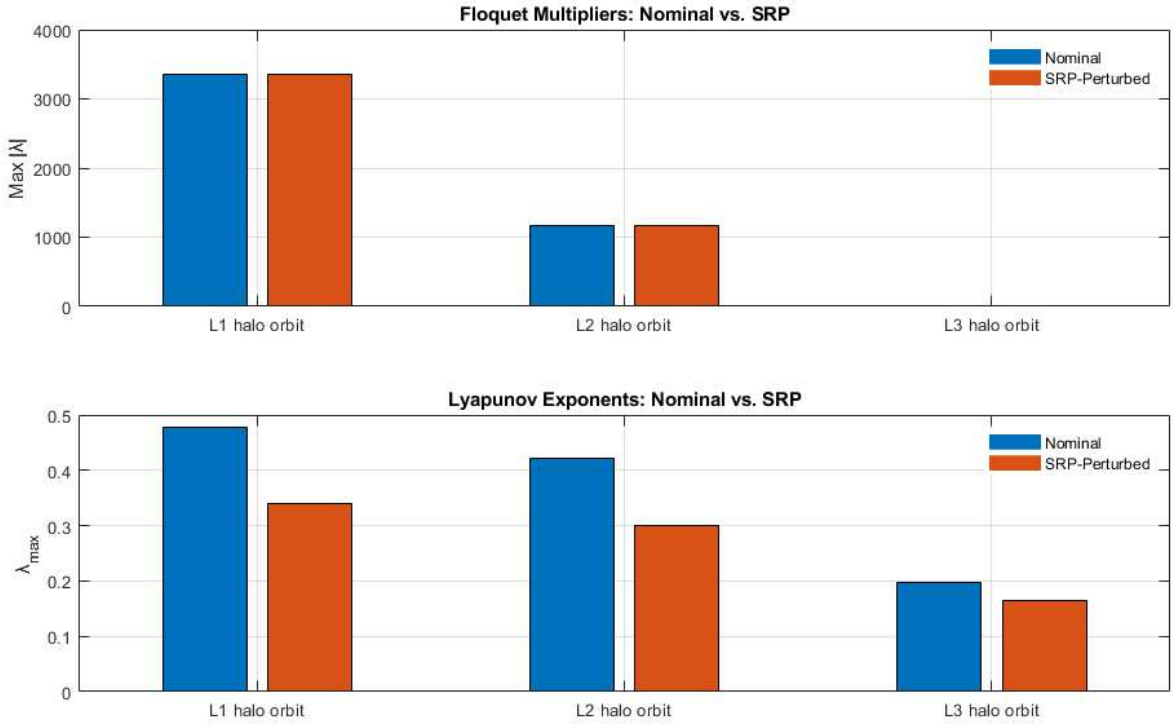


Fig. 18: Floquet Multiplier and Lyapunov exponent shifts under SRP perturbation effect

Poincaré maps for Lunar oblateness perturbed halos showed reduced chaos for L1 but increased chaotic motion for L2 and L3 halos, suggesting a more pronounced deviation from quasi-periodic motion.

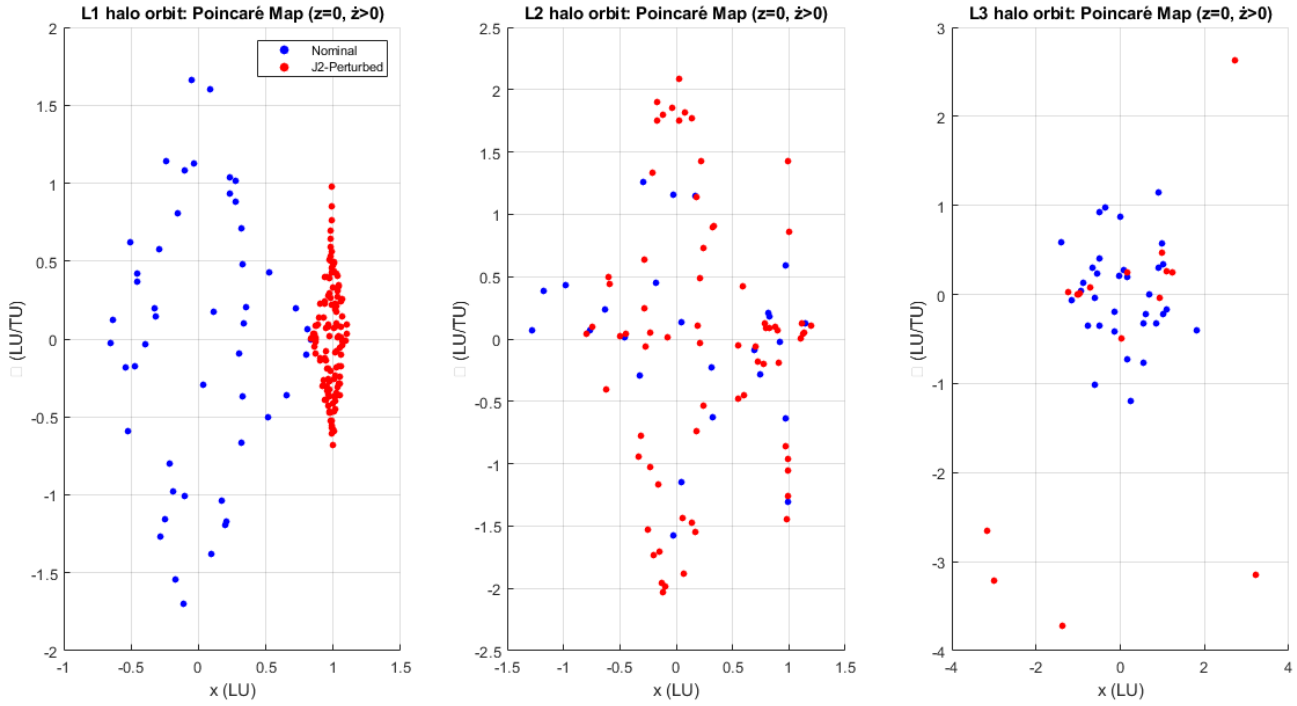


Fig. 19: Poincaré maps showing chaotic / quasi-periodic motion under Lunar J2 perturbation

All three halo orbits yield significant reduction in the maximum Lyapunov exponents, suggesting that the Lunar oblateness perturbation stabilizes the overall chaotic behavior of trajectories.

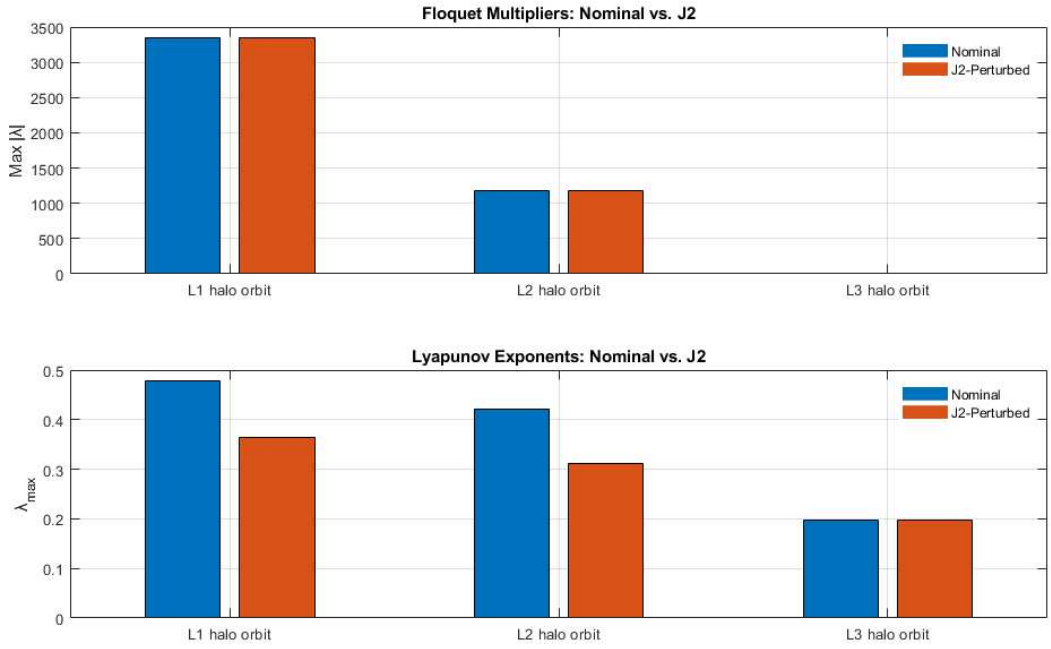


Fig. 20: Floquet Multiplier and Lyapunov exponent shifts under Lunar J2 perturbation effect

Poincaré maps for Earth Albedo perturbed halos showed similar chaotic profiles as the nominal for all three halos, suggesting minimal effect on chaotic profiles of nominal trajectories. Integration times were increased to obtain a sufficient number of crossings for accurate quantification of chaotic or quasi-periodic behavior.

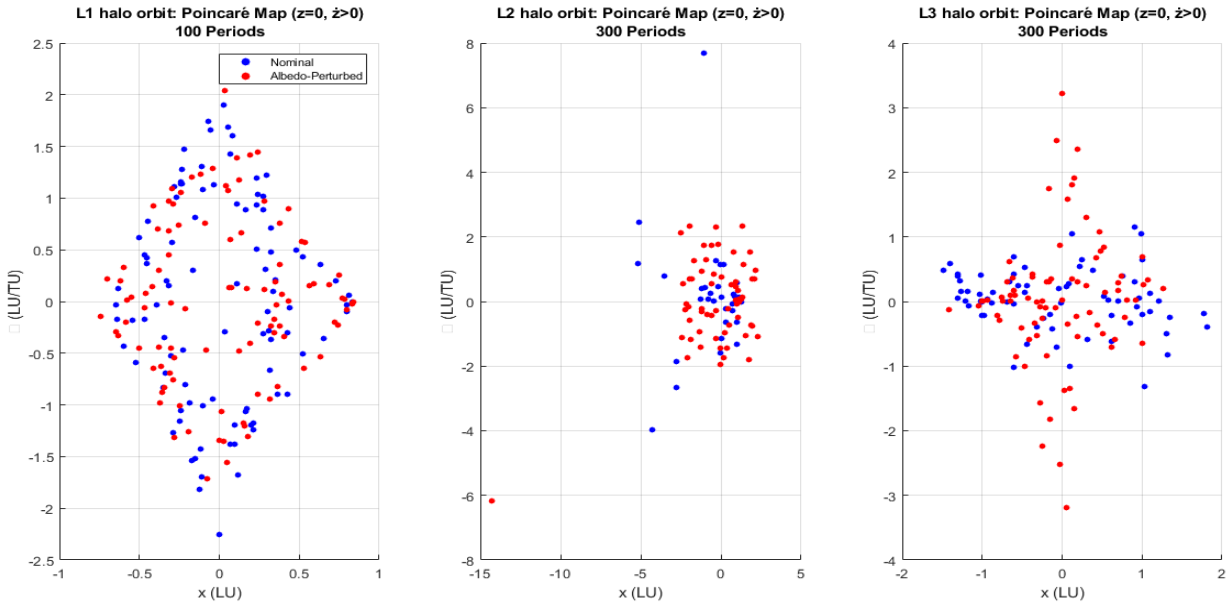


Fig. 21: Poincaré maps showing chaotic / quasi-periodic motion under Albedo perturbation

L1 and L2 halos showed a mild decrease in the maximum Lyapunov exponent under the influence of Earth's Albedo, suggesting minimal effect of Albedo in decreasing the overall chaotic divergence of trajectories. L3, however, showed no notable shift, suggesting very little or no effect on overall chaotic divergence.

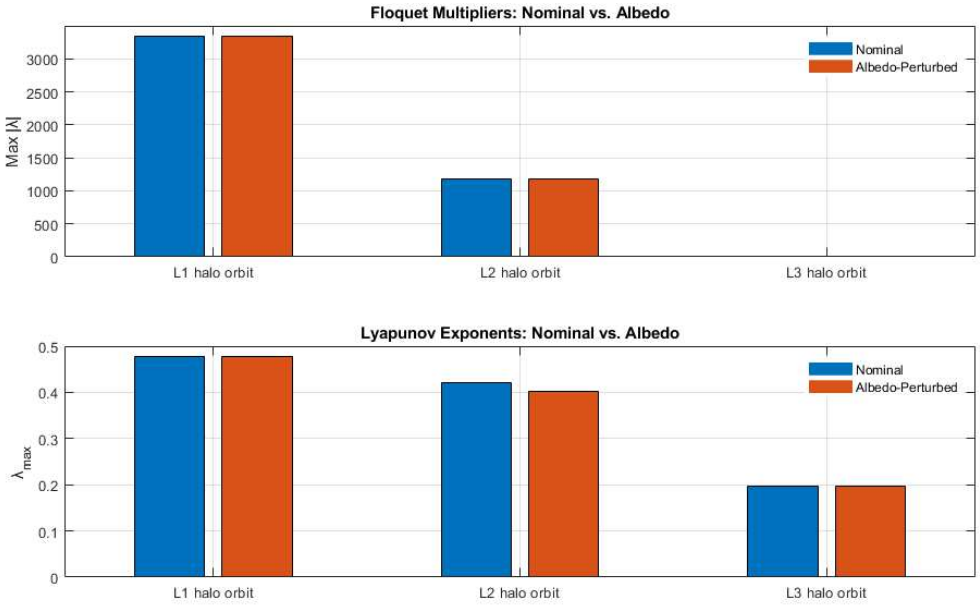


Fig. 22: Floquet Multiplier and Lyapunov exponent shifts under Albedo perturbation effect

Poincaré maps for halos under the influence of the Sun's gravity (third body) showed pronounced changes. The L1 halos exhibited strong convergence of crossing points, indicating a marked shift towards quasi-periodic motion. The L2 and L3 halos, by contrast, produced widely scattered points, indicating a rapid transition of the nominal trajectories into chaotic motion.

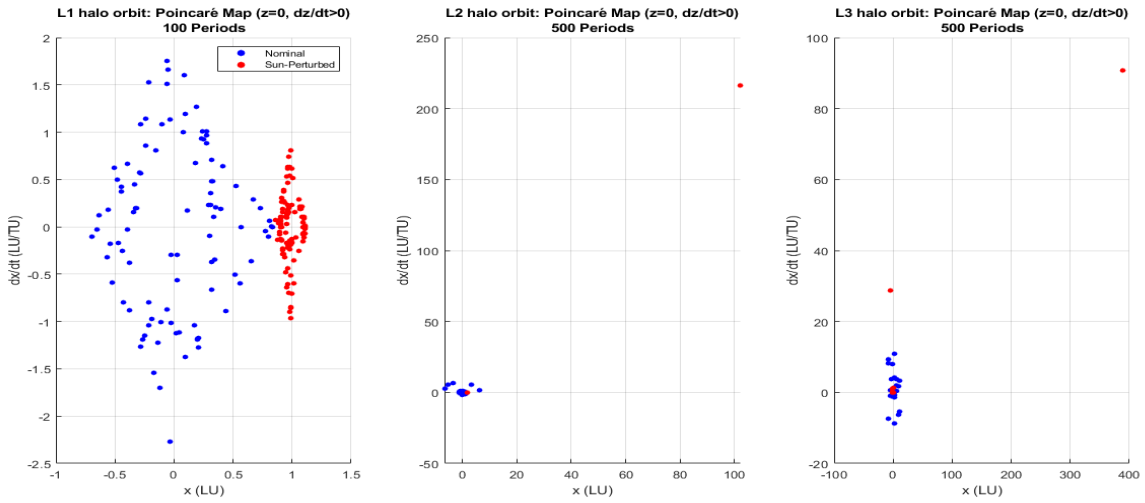


Fig. 23: Poincaré maps showing chaotic / quasi-periodic motion under Sun's gravity perturbation

Also, drastic shifts in the maximum Lyapunov exponent showed strong impact of the Sun's gravity on overall chaotic motion. All three halos showed strong decrease with respect to the nominal Lyapunov exponent, suggesting that the Sun's gravity reduces overall chaotic divergence.

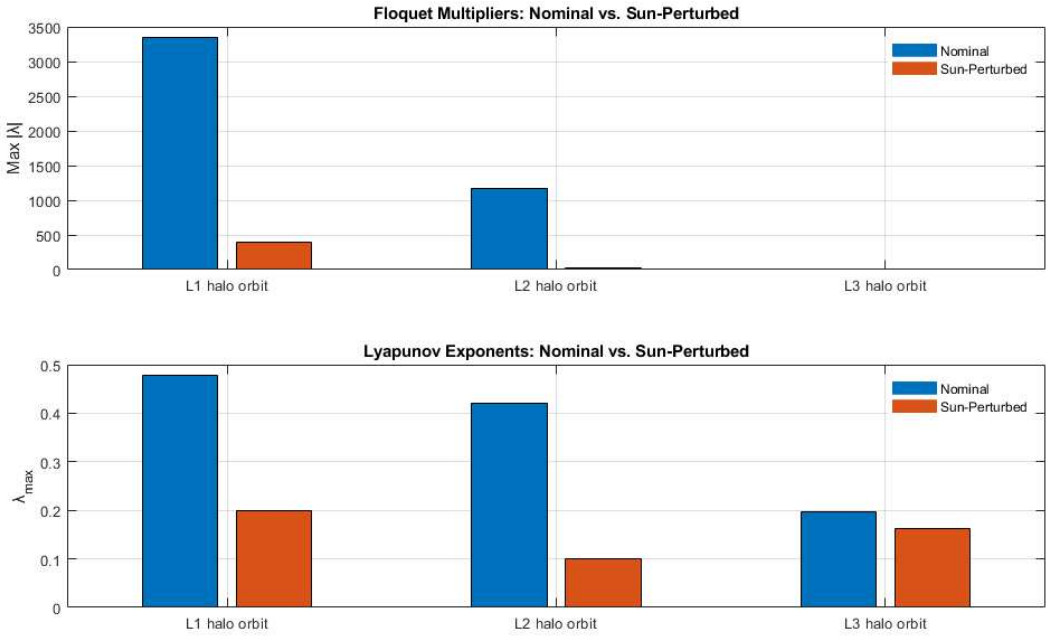


Fig. 24: Floquet Multiplier and Lyapunov exponent shifts under Sun's gravity perturbation effect

Lyapunov Exponent: Nominal vs Perturbed (λ_{max})

	Nominal	SRP	Lunar J2	Earth Albedo	Sun's Gravity
L1	0.4783	0.3390	0.3641	0.4781	0.2003
L2	0.4211	0.3011	0.3106	0.4013	0.1005
L3	0.1976	0.1638	0.1977	0.1976	0.1620

Table 7: Comparison between Nominal and Perturbed Lyapunov exponent values showing perturbation effect on chaotic divergence of trajectories.

6.6. ERROR ANALYSIS

Validation of stability results required evaluation of specific checks in halo orbit periodicity, alongside verifying that the dynamics of the CR3BP are preserved through the Jacobi-constant conservation error. The error magnitudes indicate the degree of periodicity achieved by the refined halos.

Halo orbits	Periodicity Error	ΔC_J Error
L1	3.36e-12	5.15e-14
L2	6.84e-11	2.05e-13
L3	5.20e-12	4.84e-14

Table 8: Periodicity and Jacobi-constant conservation errors of refined Halo orbits

All refined halo orbits yield extremely small periodicity errors ($\|X(T) - X(0)\| < 10^{-10}$), validating that refined halo orbits are highly periodic. Very low Jacobi-constant conservation errors ($\Delta C_J < 10^{-12}$) confirm the computational consistency of the CR3BP dynamics and demonstrate that the orbits are well corrected.

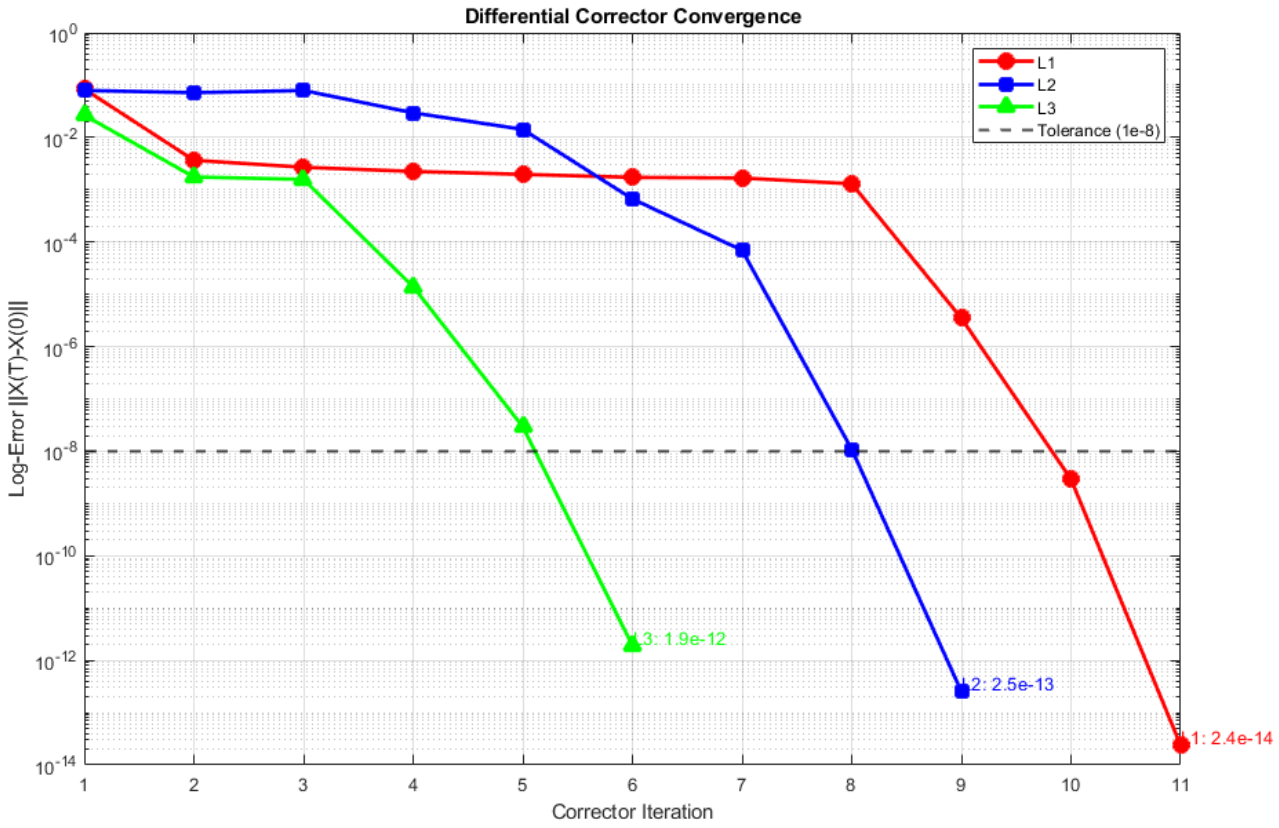


Fig. 25: Convergence of Halo Orbit differential corrector under Iterations

A Monte-Carlo analysis was also employed, in which 1000 perturbed initial conditions per orbit were sampled at a standard deviation of 10^{-6} LU across all six state components.

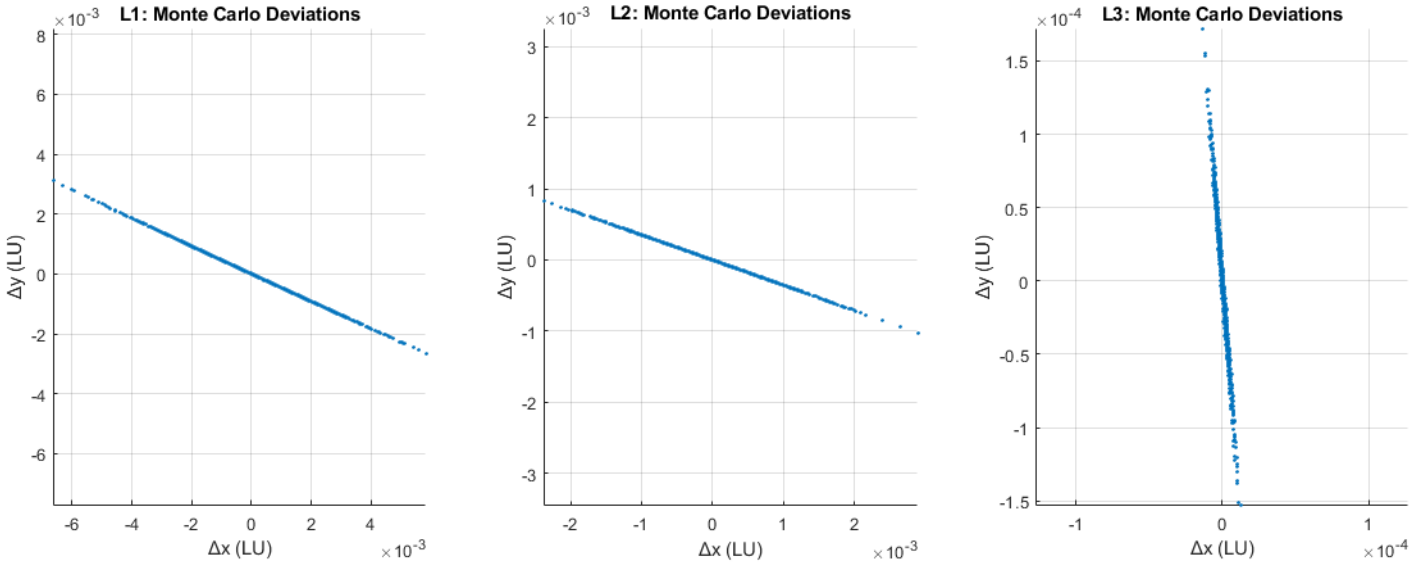


Fig. 26: Monte-Carlo Deviations plot

These maps show the spread in the stability metrics, highlighting regions of rapid transition from quasi-stable to unstable regimes, with bifurcation zones marked by clustering points near unit-circle boundaries for L1 and L2 refined halos. This reveals high sensitivity to small perturbations, where even minor deviations, say 10^{-6} in position, can amplify the Floquet multipliers by 5–15%, underscoring the sensitivity of halo orbits to small perturbations.

6.7. VALIDATION WITH EXISTING DATA AND BENCHMARKING

- The computed Floquet multipliers (e.g., $\lambda \approx 3346$ for L1) align qualitatively with Jorba and Masdemont (1999), who reported high instability in center-manifold reductions. Similarly, in comparison to Kolemen et al. (2012), our perturbation-inclusive multipliers under Sun's gravity ($\lambda \approx 398$) reveal stronger chaotic thresholds, validating the effectiveness of the method, although ephemeris-based models would be required to reproduce their quasi-periodic orbit thresholds.
- For L1 and L2 halos, the real multipliers ($\lambda > 1000$) indicate hyperbolic instability with reciprocal pairs (e.g., λ and $1/\lambda$), confirming CR3BP conservatism and exponential perturbation growth rates of $\sim\log(\lambda)/T$ per period, consistent with Richardson (1980). The complex conjugates near unity (e.g., $1 \pm 0.2i$ for L1) suggest neutrally stable oscillatory modes, potentially leading to period-doubling bifurcations as Az increases, as hinted in Kolemen et al. (2012). For L3 ($\lambda \approx 3.04$), the milder instability implies longer quasi-stable windows and correspondingly less frequent station-keeping than at L1 and L2.
- Under perturbation studies, the Sun's gravity emerges as dominant, shifting multipliers drastically (e.g., L1 from 3346 to 398), producing markedly faster trajectory divergence (Figure 15), consistent with Sheth and O (2020) in reducing stability margins under oblateness-inclusive models. In contrast, SRP and albedo induce minor shifts (<0.1%), stabilizing Lyapunov exponents (e.g., L1 from 0.478 to 0.339), suggesting they act as damping mechanisms in out-of-plane motions. J2 effects are pronounced for L1/L2 proximity to the Moon, increasing instability by ~0.05%, but negligible for distant L3.
- Under SRP perturbation, L1 maps shift from scattered (chaotic) to clustered (quasi-periodic) points, with λ_{max} dropping 29% (to 0.339), indicating perturbation-induced stabilization via reduced divergence in phase

space, contrasting Sun's gravity which scatters L2/L3 points and halves exponents (e.g., L2 to 0.1005), per Hysa (2024). This suggests SRP mitigates chaos in small-amplitude orbits, while third-body effects amplify it, leading to potential escape trajectories. J2 and albedo show minimal shifts, preserving nominal chaos levels. Overall, positive λ_{max} across cases (>0.1) confirms nonlinear instability, recommending manifold exploitation for control, as in Sato et al. (2015), to extend mission longevity in perturbed environments.

7.0 CONCLUSION AND RECOMMENDATIONS

7.1 CONCLUSION ON RESULTS AND FINDINGS

This research has conducted an extensive Floquet-based stability analysis of numerically refined halo orbits around the Earth–Moon Lagrange points L1–L3 in the Circular Restricted Three-Body Problem (CR3BP) environment. High-fidelity, high-precision true halo orbits were verified for periodicity ($\|X(T) - X(0)\| < 10^{-10}$) and for Jacobi-constant conservation ($\Delta C_J < 10^{-12}$), ensuring dynamical consistency (as described in Sections 3.3 and 6.6).

Linear stability analysis, which was centered on the Floquet multipliers and the monodromy matrix, revealed typical profiles of instability for all the Lagrange points. For the L1 halo orbits, the largest Floquet multiplier ($\lambda \approx 3346$) indicates the strongest hyperbolic instability, with perturbations diverging exponentially within a few orbital periods, as evidenced by the rapid growth of the State Transition Matrix (STM) norm and of the perturbed-trajectory divergences (Figures 7 and 8). The L2 orbits exhibited similar but somewhat weaker instability ($\lambda \approx 1176$), while the L3 orbits exhibited markedly lower instability ($\lambda \approx 3.04$), reflected in their reduced divergence rates. These values are consistent with the saddle-shaped effective potential at the collinear points, where small deviations grow exponentially and repeated station-keeping maneuvers are therefore required.

Adding the perturbative effects of solar radiation pressure, lunar oblateness, Earth's albedo and thermal radiation, and third-body solar gravity provided additional quantification of stability degradation. Solar gravity proved to be the most influential perturbation, producing large shifts in the Floquet multipliers (e.g., $\lambda \approx 398$ for L1) and rapid trajectory divergence (Figures 15 and 16), underscoring its role in long-term orbital destabilization. SRP and J2 produced more modest shifts, with SRP reducing the Lyapunov exponents (e.g., from 0.478 to 0.339 for L1), suggesting a stabilizing effect on chaotic behavior in certain regimes (Table 7 and Figure 18). Earth's albedo had little impact, as predicted from its weakness for distant halo orbits. Nonlinear testing using Poincaré maps and largest Lyapunov exponents ($\lambda_{max} > 0$ in all cases) confirmed chaotic dynamics, with perturbations such as solar gravity increasing phase-space scattering at L2 and L3 (Figure 23) while, in some cases, promoting quasi-periodic motion at L1.

Error analyses, such as Monte-Carlo simulations of initial-condition variations (Figure 26), further validated the robustness of these conclusions, exhibiting sensitivity thresholds to transitions to instability. In summary, the results establish that the L1 and L2 halo orbits are unsuitable for long-duration missions without active control, whereas L3 is comparatively quasi-stable, requiring less frequent corrections, although it is not maintenance-free. These results numerically characterize the dynamical structure of cislunar halo orbits, providing a foundation for the minimization of control effort in perturbed cases.

7.2 CONTRIBUTIONS TO ORBITAL MECHANICS AND SPACE MISSION ANALYSIS

This research makes several significant contributions to the fields of orbital dynamics and space mission design, formulating a better understanding and application of halo orbits within the Earth–Moon system.

In the first place, it provides a rigorous and comprehensive stability-analysis framework combining analytical approximations (Richardson, 1980), numerical refinement, and Floquet theory (Floquet, 1883) to enable accurate computation of monodromy matrices and multipliers for refined halo orbits (Tables 2–6). This extends previous research, e.g., Jorba & Masdemont (1999) and Kolemen et al. (2012), by integrating nonlinear descriptors (Lyapunov exponents and Poincaré sections) with linear ones, and achieving a more comprehensive description of global phase-space structures like bifurcation points and invariant manifolds. The emphasis of perturbative effects in this work bridges the gap between idealized CR3BP models and real dynamics, quantifying the extent to which forces such as SRP and third-body gravity erode stability margins, a result consistent with and extending Heiligers et al. (2015) and Dong et al. (2024).

In orbital mechanics, the incremental derivation of variational equations, STM propagation, and perturbation models (Sections 4.1 and 5.4) enhance methodological tools for periodic orbit analysis. For instance, the validation metrics (e.g., Jacobi conservation and Monte-Carlo analyses) set a benchmark for numerical accuracy in astrodynamics simulations, with possible applications to other restricted three-body problems.

For space mission design, the results have direct applications to mission planning, e.g., the Artemis Lunar Gateway at L2, by determining instability boundaries and perturbation sensitivities. Guidelines for orbit selection

(e.g., smaller-amplitude L3 halos for less station-keeping) and control strategies (e.g., using Floquet multipliers to predict divergence rates) can minimize fuel consumption and enhance autonomous navigation, echoing applications in JWST and Queqiao missions (Section 1.1). By demonstrating how perturbations like the Sun's gravity dominate instability (Section 6.4.4), the work enables risk assessment for cislunar transfers, deep-space observatories, and lunar relays, resulting in safer, more efficient mission design in an era of increasing human activity in space.

Ultimately, this work enriches the literature by providing validated, quantitative data on halo orbit stability, fostering advancements in Hamiltonian dynamics and control theory for future explorations.

7.3 RECOMMENDATIONS FOR FUTURE RESEARCH

While this study is a good beginning, certain avenues for future research can be identified to transcend its shortcomings and expand its agenda.

First, an extension of the analysis for L4 and L5 Lagrange points, which are conditionally stable ($\mu \approx 0.012 < 1/26$ threshold) and hold potential Trojan asteroids or stable orbits (Santana-Ros et al., 2022), along with comparing their Floquet stability with L1-L3 can give an insight into triangular point dynamics under similar perturbations.

Second, the application of more realistic dynamical models, i.e., the Elliptical Restricted Three-Body Problem (ERTBP) or full ephemeris integrations (e.g., DE430 models), would enable the modeling of lunar eccentricity and time-varying third-body effects (Chen et al., 2011). This would introduce perturbation realism, particularly for long-term missions where simplifying constant-Sun assumptions (Section 5.4) can lead to underestimation of instability gradients.

Third, coupling the analysis with advanced nonlinear methods, such as finite-time Lyapunov exponents or chaos indicators (e.g., Fast Lyapunov Indicators), may improve the prediction of bifurcations and long-term behavior in perturbed regimes. Combining these with machine learning for orbit correction (Sirbu and Leonardi, 2023) may automate stability mapping and find optimal initial conditions.

Fourth, control methods informed by this stability analysis, such as nonlinear model predictive control (NMPC), may prove useful for station-keeping (Berning et al., 2020), with the Floquet multipliers applied as constraints. Simulations with fuel budgets and onboard autonomy would connect theory with real-world mission scenarios such as NASA Artemis missions.

Finally, comparative studies with empirical mission data (e.g., Queqiao at L2) can complement numerical solutions, and sensitivity analyses on parameters like amplitude Az or mass ratio μ. These extensions will facilitate application in multi-body systems, supporting sustainable cislunar development.

Code Availability Statement

The code supporting this study is available on GitHub at: https://github.com/Oyefusi-Samuel/FLOQUET-LYAPUNOV-STUDY-OF-PERTURBATION-INDUCED-HALO-ORBIT

Acknowledgement

The authors of this research declare that no additional acknowledgements are necessary.

The authors also wish to state that this research did not receive any specific grant or any form of funding from agencies in the public, commercial, or not-for-profit sectors.

Ethical Declaration

The author(s) affirm that this research was carried out in compliance with ethical standards. The study did not involve human participants, animal testing, or any procedures requiring institutional ethical approval.

REFERENCES

Abouelmagd, E.I., Guirao, J.L.G. and Llibre, J. (2023) 'On the periodic orbits of the perturbed two- and three-body problems', *Galaxies*, 11(2), p. 58. Available at: https://doi.org/10.3390/galaxies11020058.

Alrebdi, H.I., Papadakis, K.E., Dubeibe, F.L. and Zotos, E.E. (2022) 'Equilibrium points and networks of periodic orbits in the pseudo-Newtonian planar circular restricted three-body problem', *The Astronomical Journal*, 163(2), p. 75. Available at: https://doi.org/10.3847/1538-3881/ac31af.

Archambeau, G., Augros, P. and Trélat, E. (2011) 'Eight-shaped Lissajous orbits in the Earth-Moon system', *Mathematics in Action*, 4(1), pp. 1-23. Available at: https://doi.org/10.5802/msia.5.

Berning, A.W., Jr., Liao-McPherson, D., Girard, A. and Kolmanovsky, I. (2020) *Suboptimal nonlinear model predictive control strategies for tracking near rectilinear halo orbits*. arXiv preprint arXiv:2008.09240. Available at: https://doi.org/10.48550/arXiv.2008.09240.

Blaga, C., Blaga, P.A. and Harko, T. (2021) *Jacobi stability analysis of the classical restricted three-body problem*. arXiv preprint arXiv:2104.02432. Available at: https://doi.org/10.48550/arXiv.2104.02432.

Burns, J.O., Mellinkoff, B., Spydell, M., Fong, T., Kring, D.A., Pratt, W.D. and Edwards, C.M. (2019) 'Science on the lunar surface facilitated by low latency telerobotics from a lunar orbital platform-gateway', *Acta Astronautica*, 154, pp. 195-203. Available at: https://doi.org/10.1016/j.actaastro.2018.04.031.

Calleja, R., Doedel, E., Humphries, A.R., Lemus-Rodríguez, A. and Oldeman, B.E. (2012) 'Boundary-value problem formulations for computing invariant manifolds and connecting orbits in the circular restricted three-body problem', *Celestial Mechanics and Dynamical Astronomy*, 114(1-2), pp. 77-106. Available at: https://doi.org/10.1007/s10569-012-9434-y.

Chen, Y., Baoyin, H. and Li, J. (2011) 'Trajectory design for the Moon departure libration point mission in full ephemeris model', *Science China Technological Sciences*, 54(11), pp. 2924-2934. Available at: https://doi.org/10.1007/s11431-011-4539-1.

Chidambararaj, P. and Sharma, R.K. (2016) 'Halo orbits around Sun-Earth L1 in photogravitational restricted three-body problem with oblateness of smaller primary', *International Journal of Astronomy and Astrophysics*, 6(3), pp. 293-311. Available at: https://doi.org/10.4236/ijaa.2016.63025.

Dong, R., Guo, H. and Liu, G. (2024) 'Comparison study of Earth observation characteristics between Moon-based platform and L1 point of Earth-Moon system', *Remote Sensing*, 16(3), p. 513. Available at: https://doi.org/10.3390/rs16030513.

Floquet, G. (1883) 'Sur les équations différentielles linéaires à coefficients périodiques', *Annales Scientifiques de l'École Normale Supérieure*, 12, pp. 47-88. Available at: https://doi.org/10.24033/asens.220.

Gao, F. and Wang, Y. (2020) 'Approximate analytical three-dimensional multiple time scales solution to a circular restricted three-body problem', *Advances in Astronomy*, 2020, p. 8868137. Available at: https://doi.org/10.1155/2020/8868137.

Haapala, A.F. and Howell, K.C. (2014) 'Representations of higher-dimensional Poincaré maps with applications to spacecraft trajectory design', *Acta Astronautica*, 96, pp. 23-41. Available at: https://doi.org/10.1016/j.actaastro.2013.11.019.

Heiligers, J., Hiddink, S., Noomen, R. and McInnes, C.R. (2015) 'Solar sail Lyapunov and halo orbits in the Earth-Moon three-body problem', *Acta Astronautica*, 116, pp. 25-35. Available at: https://doi.org/10.1016/j.actaastro.2015.05.034.

Howell, K.C. (1984) 'Three-dimensional, periodic, 'halo' orbits', *Celestial Mechanics*, 32(1), pp. 53-71. Available at: https://doi.org/10.1007/BF01358403.

Hysa, A. (2024) 'Non-linear dynamics of a test particle near the Lagrange points L4 and L5 (Earth-Moon and Sun-Earth case)', *EUREKA: Physics and Engineering*, (1), pp. 3-10. Available at: https://doi.org/10.21303/2461-4262.2024.002949.

Jorba, À. and Masdemont, J. (1999) 'Dynamics in the center manifold of the collinear points of the restricted three-body problem', *Physica D: Nonlinear Phenomena*, 132(1-2), pp. 189-213. Available at: http://dx.doi.org/10.1016/S0167-2789(99)00042-1.

Kolemen, E., Kasdin, N.J. and Gurfil, P. (2012) 'Multiple Poincaré sections method for finding the quasi-periodic orbits of the restricted three-body problem', *Celestial Mechanics and Dynamical Astronomy*, 112(1), pp. 47-74. Available at: https://doi.org/10.1007/s10569-011-9383-x.

Korneev, A. and Aksenov, S. (2021) 'Calculation of libration point orbits in the circular restricted three-body problem', *Journal of Physics: Conference Series*, 1740(1), p. 012019. Available at: https://doi.org/10.1088/1742-6596/1740/1/012019.

Langford, A. and Weiss, L.M. (2023) 'A dynamical systems approach to the theory of circumbinary orbits in the circular restricted problem', *The Astronomical Journal*, 165(4), p. 140. Available at: https://doi.org/10.3847/1538-3881/acb7df.

Lei, H. and Xu, B. (2013) 'High-order analytical solutions around triangular libration points in the circular restricted three-body problem', *Monthly Notices of the Royal Astronomical Society*, 434(2), pp. 1376-1386. Available at: https://doi.org/10.1093/mnras/stt1099.

Liu, L.B., Qian, Y.J. and Yang, X.D. (2019) 'Initial parameter analysis about resonant orbits in Earth-Moon system', *Advances in Astronomy*, 2019, p. 6324901. Available at: https://doi.org/10.1155/2019/6324901.

Marsola, T.C., Fernandes, S.S. and Balthazar, J.M. (2021) 'Station-keeping controllers for Earth-Moon L1 and L2 libration points halo orbits', *Journal of the Brazilian Society of Mechanical Sciences and Engineering*, 43(7), p. 367. Available at: https://doi.org/10.1007/s40430-021-03071-9.

Ribeiro, R.S., de Melo, C.F. and Prado, A.F.B.A. (2022) 'Trajectories derived from periodic orbits around the Lagrangian point L1 and lunar swing-bys: application in transfers to near-Earth asteroids', *Symmetry*, 14(6), p. 1132. Available at: https://doi.org/10.3390/sym14061132.

Richardson, D.L. (1980) 'Analytic construction of periodic orbits about the collinear points', *Celestial Mechanics*, 22(3), pp. 241-253. Available at: http://dx.doi.org/10.1007/BF01229511.

Santana-Ros, T., Micheli, M., Faggioli, L., Cennamo, R., Devogèle, M., Alvarez-Candal, A. ... and Weryk, R. (2022) 'Orbital stability analysis and photometric characterization of the second Earth Trojan asteroid 2020 XL5', *Nature Communications*, 13(1), p. 447. Available at: https://doi.org/10.1038/s41467-022-27988-4.

Sato, Y., Kitamura, K. and Shima, T. (2015) 'Spacecraft rendezvous utilizing invariant manifolds for a halo orbit', *Transactions of the Japan Society for Aeronautical and Space Sciences*, 58(5), pp. 261-269. Available at: https://doi.org/10.2322/tjsass.58.261.

Sheth, D. and O, T. (2020) *Halo orbits around L1 and L2 in the photogravitational Sun-Earth system with oblateness*. arXiv preprint arXiv:2003.10882. Available at: https://doi.org/10.48550/arXiv.2003.10882.

Sirbu, G. and Leonardi, M. (2023) 'Fully autonomous orbit determination and synchronization for satellite navigation and communication systems in halo orbits', *Remote Sensing*, 15(5), p. 1173. Available at: https://doi.org/10.3390/rs15051173.

Sood, R. and Howell, K.C. (2016) 'L4, L5 solar sail transfers and trajectory design: solar observations and potential Earth Trojan exploration', *Advances in the Astronautical Sciences*, 158, pp. 125-144. Available at: https://www.researchgate.net/publication/298528458_L4_L5_Solar_Sail_Transfers_and_Trajectory_Design_Solar_Observations_and_Potential_Earth_Trojan_Exploration.

Tang, H. (2019) 'Koopman-reduced order control for three-body problem', *Modern Mechanical Engineering*, 9(1), pp. 20-29. Available at: https://doi.org/10.4236/mme.2019.91003.

Wawrzyniak, G.G. and Howell, K.C. (2011) 'Generating solar sail trajectories in the Earth-Moon system using augmented finite-difference methods', *International Journal of Aerospace Engineering*, 2011, p. 476197. Available at: https://doi.org/10.1155/2011/476197.

Whitley, R. and Martinez, R. (2016) 'Options for staging orbits in cislunar space', *Proceedings of the 2016 IEEE Aerospace Conference*, pp. 1-9. Available at: http://dx.doi.org/10.1109/AERO.2016.7500635.

Williams, J., Lee, D.E., Whitley, R.J., Bokelmann, K.A., Davis, D.C. and Berry, C.F. (2017) 'Targeting cislunar near rectilinear halo orbits for human space exploration', *Advances in the Astronautical Sciences*, 162, pp. 2061-2079. Available at: https://ntrs.nasa.gov/citations/20170001352.

Yan, H. (2020) 'Port-Hamiltonian based control of the Sun-Earth 3D circular restricted three-body problem: stabilization of the L1 Lagrange point', *Modern Mechanical Engineering*, 10(3), pp. 39-49. Available at: https://doi.org/10.4236/mme.2020.103005.